Unveiling the drivers of individual critical synchronization dynamics with personalized whole-brain computational modeling

Vladislav Myrov[1†], Alina Suleimanova[1†], Paula Partanen[2], Wenya Liu[1,2], Samanta Knapič[2], Maria Vesterinen[2], Satu Palva[2,3], J. Matias Palva[1,2,3]

[1]Department of Neuroscience and Biomedical Engineering, Aalto University, Espoo, Finland
[2]Neuroscience Center, Helsinki Institute of Life Science, University of Helsinki, Helsinki, Finland
[3]Centre for Cognitive Neuroimaging, School of Neuroscience and Psychology, University of Glasgow, Glasgow, UK

***For correspondence:**
vladislav.myrov@aalto.fi (VM)

[†]These authors contributed equally to this work

Abstract

Personalized whole-brain computational modelling of emergent brain dynamics, where the models are fitted with individual experimental data, has become increasingly important for understanding the systems-level mechanisms governing large-scale brain activity in health and disease. Healthy brain dynamics is characterized by oscillatory synchronization and brain criticality, which are fundamental for cognitive functions. Abnormal dynamics likely has a mechanistic relationship with several brain disorders. Current modelling and model fitting approaches reconstruct well the individual functional-connectivity patterns observed, *e.g.*, in fMRI. However, there are no model-fitting approaches that would yield personalized models with *in-vivo*-like critical synchronization dynamics observable with electrophysiological methods. Here, we advance a new Hierarchical Kuramoto model, of which the simplest realization has two layers and comprises a network of nodes that each contain a large number of coupled oscillators. Already at two levels of hierarchy, this model enables explicit representation of local and inter-areal coupling and observations of emergent multi-scale synchronization dynamics. We show here that the model produces biologically plausible meso- and macro-scale synchronization dynamics and is directly comparable with electrophysiological magneto- and electroencephalography (M/EEG) data. We then advance a novel approach for fitting this model with individual experimental data, which uses not only functional connectivity but also criticality to obtain personalized model parameters with individual M/EEG and structural-connectivity. We posit that models with personalized brain synchronization dynamics will support both clinical applications and basic research on the systems-level mechanisms of cognitive functions. The model and model-fitting approach advanced here open new avenues for mechanistic understanding of experimental observations and generation of testable predictions for future research.

Introduction

Healthy brains exhibit dynamics characterised by moderate levels of long-range phase synchronization (***Pusil et al.*** (***2019***); ***Alamian et al.*** (***2017***); ***Hirvonen et al.*** (***2017***); ***Fuscà et al.*** (***2023***)), which is fundamental for neuronal communication in brain networks (***Fries***

(*2015*)) and the cognitive functions achieved therein. Accordingly, several lines of cognitive tasks are associated with dynamic patterns of long-range synchronisation linking task-relevant cortical areas (**Palva et al.** (**2010a**); **Haque et al.** (**2020**); **Siebenhühner et al.** (**2016**)). Abnormal synchronization, on the other hand, characterizes neuropsychiatric diseases such as depression, where abnormalities in synchrony are correlated with the severity of depression symptoms (**Zhang et al.** (**2016**); **Kaiser et al.** (**2015**); **Mohammadi and Moradi** (**2020**)), and constitutes a core mechanisms for neurological disorders such as epilepsy (**Wang et al.** (**2023a**); **Arnulfo et al.** (**2020**)) and Parkinson's disease (**Boon et al.** (**2019**)).

Neuronal oscillations exhibit considerable variability in characteristics such as frequency, power, or synchronisation, and the variability therein is associated with differences in cognitive performance (**Palva et al.** (**2010b**); **Pusil et al.** (**2019**); **Simola et al.** (**2022**)), learning (**Micou and O'Leary** (**2023**)), or neurological state (**Wang et al.** (**2023a**)). The framework of criticality provides an approach to understanding this variability: the "critical brain" hypothesis (**Shew and Plenz** (**2012**); **Chialvo** (**2010**)) proposes that the Operating Point (OP) of neuronal systems *in vivo* lies near the critical transition between the subcritical and supercritical phases of the system's state space. Operation near the critical phase transition gives rise to the emergence of scale-free spatio-temporal correlations, observable both as long-range temporal correlations (LRTCs, **Linkenkaer-Hansen et al.** (**2001a**)) and power-law scaled avalanches (**Beggs and Plenz** (**2003**)), and yields several functional advantages, such as maximized information capacity (**Shew and Plenz** (**2012**)), information complexity (**Lotfi et al.** (**2021**)), information processing(**Kinouchi and Copelli** (**2006**)), dynamic range and transmission rate (**Zimmern** (**2020**); **Heiney et al.** (**2021**)).

The Operating Point is a position in the state space and is determined by the system's control parameters. In neuronal systems could exist several control parameters such as the excitation-inhibition (E/I) balance (**Beggs** (**2007**)) or cellular-level mechanisms (**Shine et al.** (**2021**)). A given OP is associated with specific emergent dynamics, which can then be operationalized with a range of synchronization and criticality observables (**Linkenkaer-Hansen et al.** (**2001a**); **Beggs and Plenz** (**2003**); **Poil et al.** (**2012**); **Fuscà et al.** (**2023**); **Palva et al.** (**2013**)). In recent research it was shown with stereo-EEG (SEEG) and MEG that individual levels of phase synchronization are determined by brain criticality in a manner consistent with a hypothesis that structural heterogeneity stretches the critical point into a extended regime of critical-like dynamics, the Griffiths phase (GP), and individual OPs exhibit wide variability across the GP (**Fuscà et al.** (**2023**)). Because neither the control parameters nor system states are readily observable with experimental methods, their *in vivo* relationships with state observables (such as synchrony, LRTCs, and avalanches) have remained a topic where computational modeling is essential for mechanistic understanding.

In prior art, a number of computational models have been advanced to study mechanistical princples underlying the whole-brain neural dynamics (**Ritter et al.** (**2013**); **Ponce-Alvarez and Deco** (**2024**); **Breakspear et al.** (**2010**)) and phase synchronization among neuronal population oscillations in particular, such as the Wilson-Cowan model (**Cowan et al.** (**2016**)), Neural Mass model (**David and Friston** (**2003**)), Hopf model (**Cabral et al.** (**2022**)) or Kuramoto model (**Schmidt et al.** (**2019**); **Pang et al.** (**2021**)). Computational models have also been used in criticality research, for example for studying avalanches using branching-process (**Hobbs et al.** (**2010**)) and Ising models (**Liu and Dahmen** (**2009**)) from statistical physics as well as neurophysiology-inspired population models (**Aburn et al.** (**2012**); **Deco et al.** (**2017**); **Roberts et al.** (**2019**)) and networks of excitatory and inhibitory neurons (**Poil et al.** (**2012**)). LRTCs have been found, e.g., in the critical oscillations (CROS) model (**Avramiea et al.** (**2022**); **Dalla Porta and Copelli** (**2019**)) and neuromorphic models (**Shirai et al.** (**2020**)).

The Kuramoto model is the simplest model of synchronization dynamics and captures the emergence of synchrony in a system of coupled oscillators. The Kuramoto model yield both *in-vivo*-like LRTCs (**Fuscà et al.** (**2023**)) and avalanches (**Villegas et al.** (**2014**)). The model exhibits a transition between subcritical (asynchronous) and supercritical (synchronous) phases, which is characterised by emergence of critical-like dynamics with power-law long-range correlations. In the classical definition of the Kuramoto Model, its dynamics is controlled by a single parameter – the coupling strength between oscillators. In prior research using Kuramoto modeling in the neuroscience context the activity of a local neuronal population (cortical parcel) has been represented by a single Kuramoto (**Koller et al.** (**2024**)) or Hopf oscillator (**Deco et al.** (**2021**)), making it impossible to leverage the criticality framework for node-level observables. This has led us to advance the Hierarchical Kuramoto model where local activity is modeled with large numbers of oscillators in small networks (**Siebenhühner et al.** (**2020a**)) or in theoretical settings with complete white-matter connectomes (**Fuscà et al.** (**2023**)).

The models invariably, however, have large numbers of parameters and only a small fraction of their parameter space is associated with biologically relevant dynamics. This is crucial because the models yield biologically relevant model predictions and mechanistic understanding exclusively in such dynamic regimes. Several studies have initialized mean-field model parameters with experimen-

tal biological constraints on micro-scales, such as synaptic current kinetics, and on macro level, like with an connection weight matrix between Kuramoto model nodes (***Schmidt et al.*** (***2015***)), connectivity structure (***Ódor and Kelling*** (***2019***)) or interaction delays estimated from the tract lengths (***Ziaeemehr and Valizadeh*** (***2021***)) using the human structural connectome. However, most model parameters might not match with experimental observables and some of these observables might simply not be available in human experiments.

Over the past decade, "model fitting" has emerged as a new paradigm to overcome this challenge and to concurrently obtain personalized models and models that express biologically realistic dynamics. Model fitting is an inverse process that aims to discover the model parameters that yield the best agreement between the model and real data observables. In a leading example of this approach, the models are fitted to a (time-averaged) functional connectome derived from fMRI time-series, e.g., with correlation coefficients of BOLD signals (***Deco et al.*** (***2013***); ***Wang et al.*** (***2019***); ***Schirner et al.*** (***2023***)). A few studies have applied model fitting also to MEG/EEG source signals and used amplitude cross-correlation profiles (***Castaldo et al.*** (***2023***)), time-lagged interactions (***Heggli et al.*** (***2019***)), or long-range phase synchronization matrices (***Williams et al.*** (***2023***)) as the fitting target.

Model fitting can be done from different angles, and the process of Bayesian optimization has shown a promise in recent studies (***Hashemi et al.*** (***2020***); ***Lintusaari et al.*** (***2016***); ***Gutmann et al.*** (***2016***)), particularly based on Dynamic Causal Modeling (DCM, ***Wang et al.*** (***2019***)). Evolutionary algorithms have also been used to fit avalanche size and duration distributions, and LRTCs, with empirical data as a function of connectivity parameters (***Avramiea et al.*** (***2022***)). These approaches are universal and can be used applied to essentially any modelling scheme but adapting them to personalized whole-brain models is an insurmountable task because of the large number of learnable parameters, which makes the optimization convergence impossible or impractically slow.

Another way of fitting a model is to rely on a-priori knowledge about the relations between a model parameters and observables, for example, so that the fitting process assumes that functional connectivity increases monotonically as a function of a coupling control parameter and thus the gradient for these parameters can be obtained as a difference between an actual and predicted connectivity values. In contrast, fitting to criticality properties poses a more challenging task and has been done only using an evolutionary method in application to LRTCs in spiking models ***Avramiea et al.*** (***2022***). To the best of our knowledge, no existing work has explored how to perform this fitting process for oscillations, particularly the co-fitting of criticality and the functional connectome although both theoretical and in-vivo evidence show they are intertwined ***Fuscà et al.*** (***2023***).

We posit here that development of truly personalized oscillatory models requires solving two problems. The first is to create a model that yields both dynamics and observables that are sufficiently similar to real data, allowing for direct comparison between simulated and real brain recordings. This includes also the notion that the model ideally produces the targeted phenomena (synchronization dynamics in the present context) with a minimal amount of parameters and model details. The second is to develop an algorithm that co-fits the model with multiple observables of brain dynamics, including both connectivity and criticality observables, such as the functional connectome and long-range temporal correlations.

In the present study, we advance a hierarchical extension of the classical Kuramoto model with two levels of hierarchy. On the first level, basic functional units – oscillators – are grouped into a single node, on the second level those nodes are organized into a network. Following this architecture, the dynamics of a single oscillator has three parts: the natural dynamics or the oscillation frequency, internal dynamics dictated by phase difference between oscillators in the same same node and external dynamics based on the phase difference with other nodes. We posit that the hierarchical architecture has several advantages, including that each model node can be directly mapped to an brain parcel, which enables local and inter-areal synchronization dynamics observables to be directly comparable with those of real data. Enables the inclusion of structural-connectivity driven heterogeneity in the model, which gives rise to an extended critical regime even on node level. From the technical side it encapsulates individual oscillator interactions inside each node and allows to improve computational performance and makes easier to extend the model for additional features such as delayed phase-interactions without changing the whole model code.

For model fitting, we introduce here a new dual-gradient descent approach. The control parameters of the Kuramoto model (local and inter-areal coupling) have a sigmoid-like relationship with phase-synchrony, which enables gradient-descent model fitting so that the difference between actual and predicted phase synchronization can be used as a gradient to adjust the coupling strength (***Deco et al.*** (***2019***); ***Schirner et al.*** (***2023***)). However, criticality, as operationalized with LRTCs and the DFA scaling exponent, for example, has a quadratic relationship with the control parameters so that the LRTCs are strongest at the phase transition. We use here a new approach where the LRTCs are approximated with a gaussian function and optimized as a function of the local control parameter.

We demonstrate that by combining these two approaches, the model can simulate realistic-like brain synchronization dynamics at the phase transition between order and disorder. We compared the simulated timeseries with real data and demonstrated that the models from the subcritical slope of the Griffiths Phase yield the most physiologically plausible and similar to the MEG-derived observables. Finally, we show that model fitting algorithm can learn both critical and synchrony properties simultaneously, successfully restores artificially generated phenotypes with known parameters and a fitted model can reproduce critical and phase synchrony profiles of real brain neuronal dynamics.

Results

Whole-brain model of critical oscillations

Neuronal oscillations are rhythmic excitability fluctuations and occur in the brain across a wide frequency range. Oscillations are a fundamental element of brain dynamics arising from the frequency-specific synaptic interactions within neuronal micro- and macrocircuits ***Buzsáki et al.*** (***2012***). The standard operationalization of human neuronal oscillations uses electroencephalography (EEG), stereo-EEG (SEEG), and/or magnetoencephalography (MEG) (Figure 1A, ***Brookes et al.*** (***2011***)). Their sensor-level recordings are collapsed into cortical parcellations, and the parcel time series are filtered to obtain narrow-band analytical time series (See Figure 1B) and observables such as power spectra (See Figure 1C), amplitude correlations (See Figure 1D,F), and phase synchrony (See Figure 1E,G) that quantify neural dynamics constructs like functional connectome, rhythmicity or criticality.

The local field potentials are generated by collective activity of multiple neuronal cells ***Buzsáki et al.*** (***2012***) and oscillations emerge from time-aligned – rhythmical – neuronal activity which may be approximated using periodic functions. Analogous to a cortical area containing many small sub-populations of neurons, a single model node contains many Kuramoto oscillators ***Kuramoto*** (***1975***); ***Siebenhühner et al.*** (***2020a***), which are directionally coupled within a node weighted by local control parameter (K , See Figure 1H). Similar to amplitude, which operationalizes local neuronal activity within a population, we operationalize node order as an agreement of oscillators phases measured with an average complex value across oscillators, resulting in an complex time series with high amplitude when oscillators are synchronized and low when their phases are distributed across the unit circle (See Figure 1H).

On the next level of hierarchy, model nodes, the coupling is based on directional phase-difference weighted by node order and a structural edge weight between two nodes (See Figure 1I, see Methods for details). This approach encapsulates interaction between different levels of hierarchy, induces an additional level of heterogeneity in the model, and allows to reduce computational costs. It also gives a rise to naturalistically-looking model time series with observables such as amplitude and phase that are easily comparable to narrow band real data (See Figure 1 I) as well as uni- and bivariate statistics such as Power Spectrum (See Figure 1 J), Amplitude Correlation (See Figure 1 K,M) and Phase Synchrony (See Figure 1 L,N).

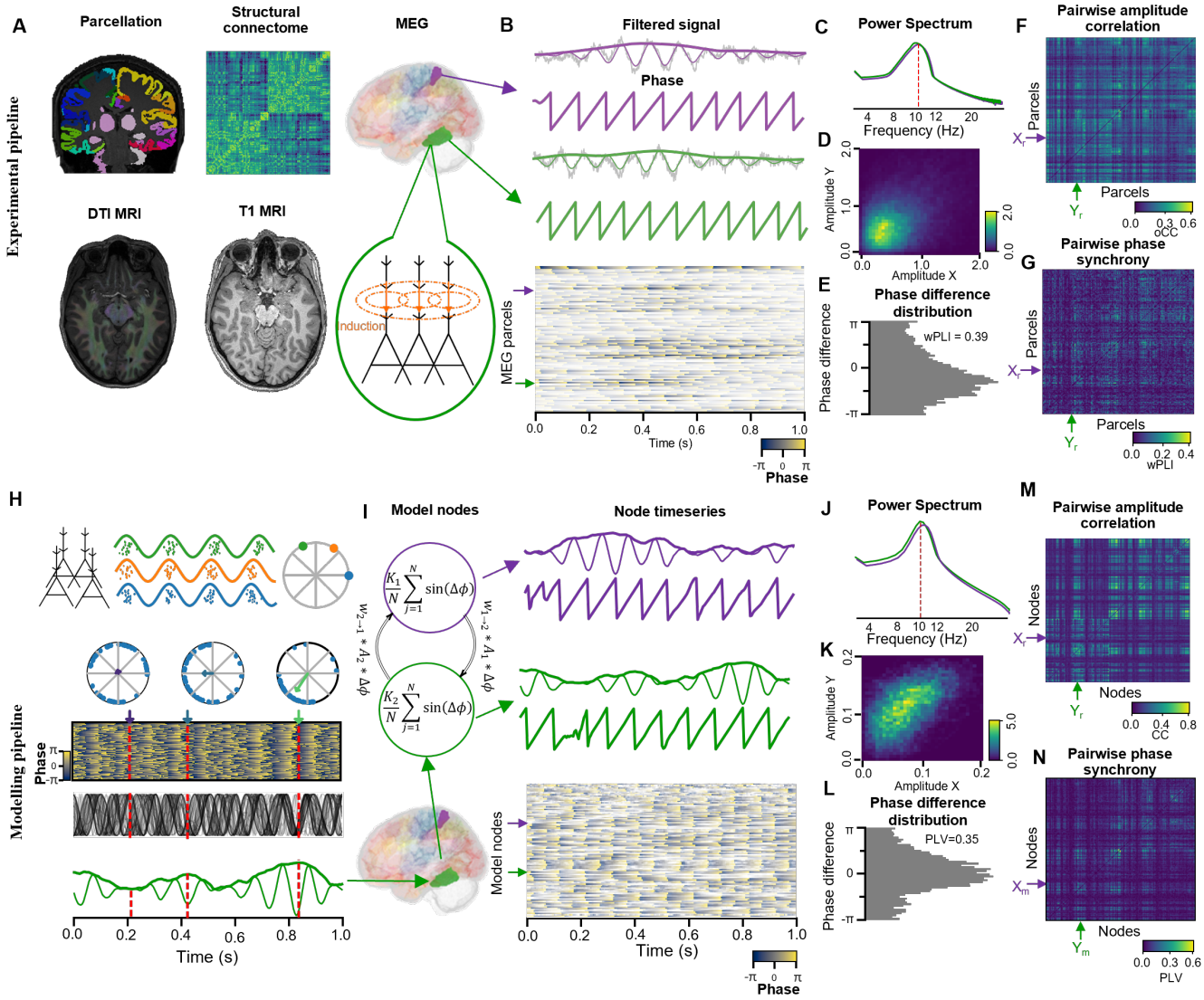

Figure 1. General representation of an experimental pipeline. **A** Examples of the imaging methods (T1 MRI, DWI MRI, MEG) and their derivatives (MRI-based parcellation, structural connectome based on DWI) used in this study. **B** Broadband MEG time series from two parcels (gray) overlaid with the real part of the narrow-band filtered data and its phase. On the bottom, the heatmap of channel phases where samples with low amplitude are transparent. **C** Power Spectrum for two parcels in MEG data. **D** 2D histogram for amplitude of two narrow band MEG signals. **F** Pairwise amplitude correlation heatmap of MEG narrow-band data. **E** Distribution of phase differences for a pair of narrow band MEG signal. **G** Pairwise wPLI of single-subject MEG recording at alpha frequency (10Hz). **Modelling pipeline**. **H** The spiking process of a neuronal population could be approximated using a periodic function in complex space or oscillator. Hundreds of interacting oscillators represent a single model node and their phases are averaged on each time point to obtain a timeseries of a node timeseries. **I** Two-node model scheme with equations for coupling within a node and between them. **J** Power Spectrum obtained from the real part of a simulated timeseries. **K** 2D histogram for amplitude of two simulated timeseries. **M** Pairwise amplitude correlation heatmap of simulated data. **L** Distribution of phase difference for two simulated signals. **N** Pairwise PLV matrix of a simulated timeseries

Local and global control parameters shape the criticality landscape of the model dynamics

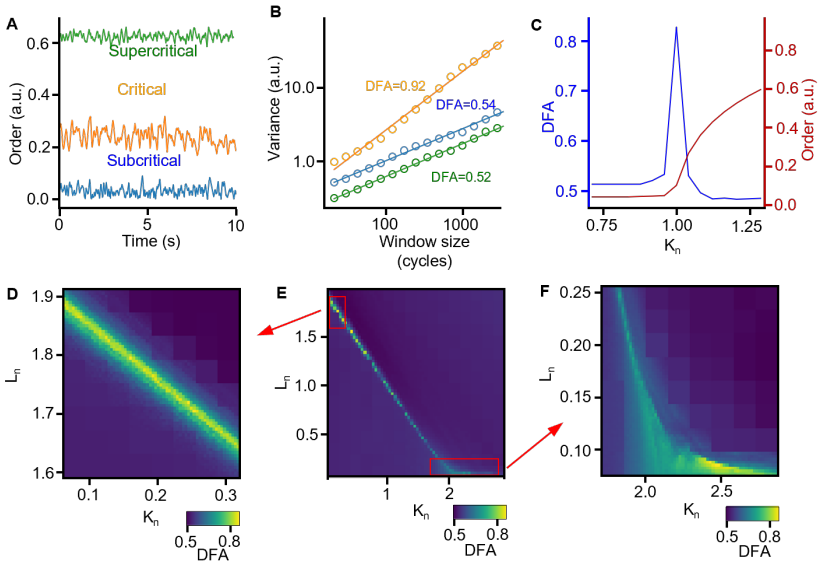

Figure 2. The critical landspace as a function of local and global control parameters. **A** Example simulated time series for the subcritical, critical and supercritical model dynamics. **B** Variance as a function of window size for the example time series shown in **A** and their Detrended Functional Analysis (DFA) fits. **C** An average model DFA and order as a function of a local control parameter normalized by the K with the maximum DFA. **D, E, F** DFA as a function of both local and global control parameters for the region with $K_n \ll L_n$ (**D**), K ~ L (**E**), $K_n \gg L_n$ (**F**).

Brain activity exhibits a $\frac{1}{f}$-like power spectrum and spatiotemporally scale-free dynamics, which have been attributed to brain-criticality. According to the 'critical brain' hypothesis, neuronal systems in vivo operate at the critical transition between subcritical and supercritical states in the system's state space (Figure 2A). In oscillatory network models criticality occurs between desynchronization and complete synchronization on both nodal and inter-node level, operationalized with node order and inter-node phase synchronization, respectively. This critical regime is characterized by Long Range Temporal Correlations (LRTCs) which can be operationalized using the detrended fluctuation analysis (DFA, See Figure 2B).

However, in previous research, oscillatory models of brain activity assigned a single oscillatory unit to an anatomical region, thus they were unable to reproduce critical dynamics of individual brain zone because the order remained constant across time. In the hierarchical Kuramoto model, each node may have thousands of oscillators whose phases are averaged to obtain node time series. Due to differences in natural frequencies of oscillators and non-linear interactions, the node timeseries vary in time and long-range temporal correlations emerge in the critical state. We found this approach makes it possible to capture the critical transition between disorder and order on a singe-node level and this transition is characterized by a peak in the DFA scaling exponent, indexing high criticality (See Figure 2C).

To assess how model parameters affect the criticality properties of the model, we varied both local and global control parameters, simulated a 5-minutes long time-series for each pair of parameters (not counting the warm-up period of 60 seconds) and computed the DFA exponent for simulated time-series as a function of control parameters. For visualization purposes, to negate the effect of other simulation arguments such as amount of noise or the scaling of control parameters, we selected a K & L pair which were as close as possible and located on the critical ridge, divided the actual the actual values on it to obtain a normalized local (K_n) and global (L_n) coupling weights.

Varying both local and global control parameters, we found that the critical landscape is divided into subcritical and supercritical parts by a critical ridge which has linear shape when K is much lower than L (See Figure 2D) or close to L (See Figure 2E). In contrast, the critical surface becomes non-linear when global connectivity is low while local is high (See Figure 2F), which can be attributed to increased contribution of variation in local node order which influences an inter-node directional coupling.

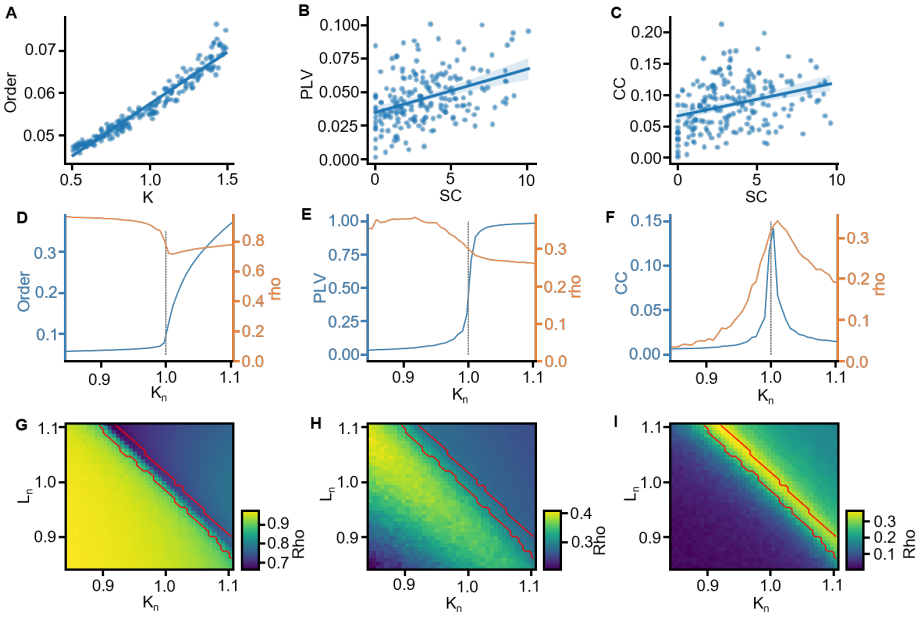

Figure 3. The linear correlations break at the model critical point. **A, B, C** Examples of model Order , PLV and Order Cross-Correlation as a function of local control parameter (K) and Structural Connectivity (SC). **D** Pearson Correlation Coefficient between model Order and K, **E** PLV and SC, **F** CC and K as a function of normalized local control parameter (Kn). **G** Pearson correlation coefficient between model Order and K, **H** PLV and SC, **I** CC and K as a function of both Kn and normalized global control parameter (Ln). The red lines indicate the critical ridge location estimated from the average CC value across nodes (Supplementary Figure 1).).

Correlation between model parameters and observables is modulated by critical properties

In critical-like systems with a second order phase transition, the order as a function of the control parameter follows an S-like shape and the critical observables peak in the phase transition region known as the Griffiths phase. Previous studies have shown that DFA has a negative quadratic correlation with phase synchrony in the critical region and a linear correlation otherwise ***Fuscà et al.*** (***2023***). However, the relationships between the underlying model parameters and the observed model dynamics are not clear.

To assess the relationships between the model's control parameters and its observables, we sampled the local coupling coefficient for each node and inter-node weight for each edge from the uniform distribution (minimum=0.5, maximum=1.5), multiplied them on varied local and global control parameters and simulated a 5-munutes long time-series. For each simulation we calculated the order, the phase locking value (PLV) and the cross-correlation (CC) between the time series envelopes, and assessed the relationships between order and local K (Figure 3A), PLV, CC and local L (See Figure 3B, C) using the Pearson correlation coefficient.

Initially we found that all observables have a non-negative correlation with the control parameters, but the shape of these correlations is different. First of all, model local and inter-nodal synchronization has a linear-like structure function relationship with the control parameters in the subcritical regime which breaks around the critical point. The order has the highest correlation with K in the subcritical region (Pearson coefficient $\sim 0.9, K_n < 1.0$), drops in the critical state (Pearson coefficient $\sim 0.6, K_n \sim 1.0$) and starts to increase in the supercritical, but is still lower compared to the subcritical region (Pearson coefficient $\sim 0.7 - 0.8, K_n > 1.0$, See Figure 3D).

The correlation of the phase synchrony with the control parameters has a similar behaviour to the order, with maximum values in the subcritical zone (Pearson coefficient $\sim 0.4, K_n < 1.0$), which decreases around the critical zone (Pearson coefficient $\sim 0.25, K_n \sim 1.0$), but then continues to decrease and reaches the minimum values at the end of the K_n range (See Figure 3E).

On the other hand, the correlation between CC and control parameters has a completely different shape from that of order and PLV: it is almost non-existent for the lower part of the subcritical region (Pearson coefficient $\sim 0.0, K_n < 0.9$), starts to increase approaching the critical region (Pearson coefficient $\sim 0.1, 0.9 < K_n < 1.0$), peaks at criticality (Pearson coefficient $\sim 0.3, K_n \sim 1.0$), begins to slowly decrease in the super-critical region, but remains higher than in the subcritical region (Pearson coefficient $\sim 0.2, K_n > 1.0$, See Figure 3F).

Spectral properties of oscillatory activity are defined by distribution of underlying frequencies

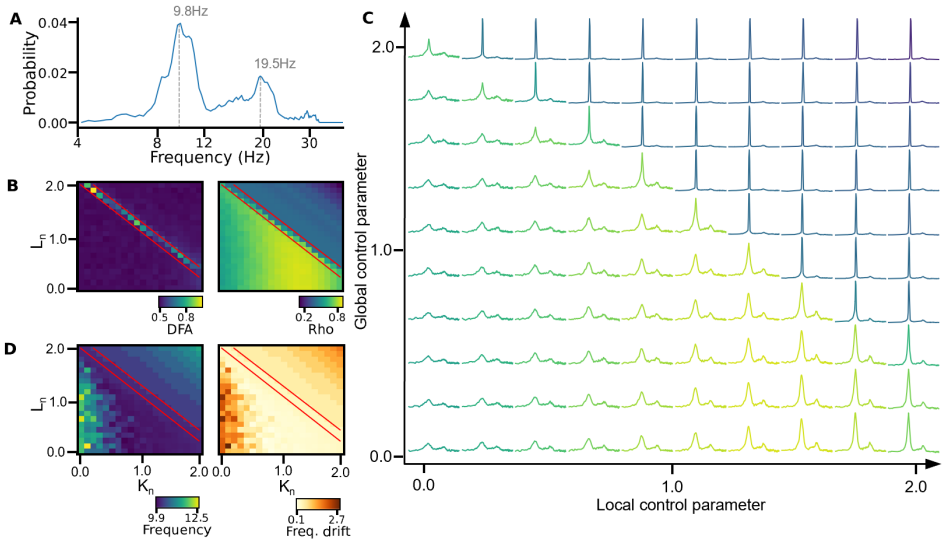

Figure 4. Oscillator frequencies shape the power spectrum. A distribution of oscillator frequencies obtained from individual power spectral density of a real MEG recording with subtracted $\frac{1}{f}$ component. **B** Average detrended fluctuation analysis (DFA) exponent across model nodes (left) and Pearson correlation coefficient between PSD of a real and simulated timeseries (right) as a function of normalized global (L_n) and local (K_n) control parameters. The red lines indicate a criticality ridge estimated with DFA exponent ≥ 0.65. **C** PSD of simulated timeseries for different combinations of local and global control parameters colored by their correlation with the PSD of the real data as shown in **B**. **D** A frequency peak derived from power spectrum of simulated timeseries (left) and difference with the peak location in the distribution of oscillator frequencies (right).

Traditionally, oscillations are operationalized by their magnitude and studied through power spectral techniques, wherein a spectral peak above the "$\frac{1}{f}$" aperiodic component serves as the definitive benchmark indicating the existence of oscillations ***Buzsáki et al.*** (***2012***). In human MEG - EEG recordings power spectrum typically has a peak in alpha (7–14Hz) or beta (14–30Hz) frequencies ***Buzsáki*** (***2006***) and the shape of the power spectrum depends from various factors such as cell firing rate ***Manning et al.*** (***2009***), stimuli representation ***Mazzoni et al.*** (***2008***), cognitive state ***Haegens et al.*** (***2014***) or mental disorders ***Ippolito et al.*** (***2022***). Therefore, plausibly-looking power spectrum is an important aspect of any oscillatory model.

In order to replicate the individual power spectral properties of a subject in a model, we initialized the distribution of oscillator frequencies to match the shape of power spectrum of a recording. To achieve this, we first computed the power spectrum density (PSD) of the MEG recording, subtracted the $\frac{1}{f}$ component from it using the FOOOF method ***Donoghue et al.*** (***2020***) and transformed it into a probability distribution of oscillator frequencies by dividing on cumulative sum (Figure 4A). The local coupling strength was set to the constant value across nodes and the inter-edge weights were sampled from a uniform distribution and divided on the mean value to preserve the mean value of one.

To assess the similarity between real and simulated data, we varied the local (K) and global (L) control parameters, ran a 360-seconds long simulation, cut-off the first 60 seconds to remove the warm-up periods, computed PSD of the simulated data using the Welch method and the pearson correlation coefficient between the real-data and model power spectra. We found that the maximum correlation coefficient is located in the subcritical slope of the extended critical zone with high local control parameter and low global (See Figure 4B).

The transition from subcritical to critical regime is characterized by emergence of oscillatory peaks which are almost absent low control parameters but are raising as control parameters grow towards the critical ridge and the alpha peak becomes dominant closer to the critical zone (See Figure 4C). Interestingly, the critical and the subcritical regimes with high global control parameter (L) exhibits a small drift of the alpha frequency peaks towards the weighted mean (12.85Hz) of alpha (9.8Hz) and beta (19.5Hz) frequency peaks (See Figure 4D), and the high correlation between the simulated and observed power spectrums could be explained by alignment of such peaks.

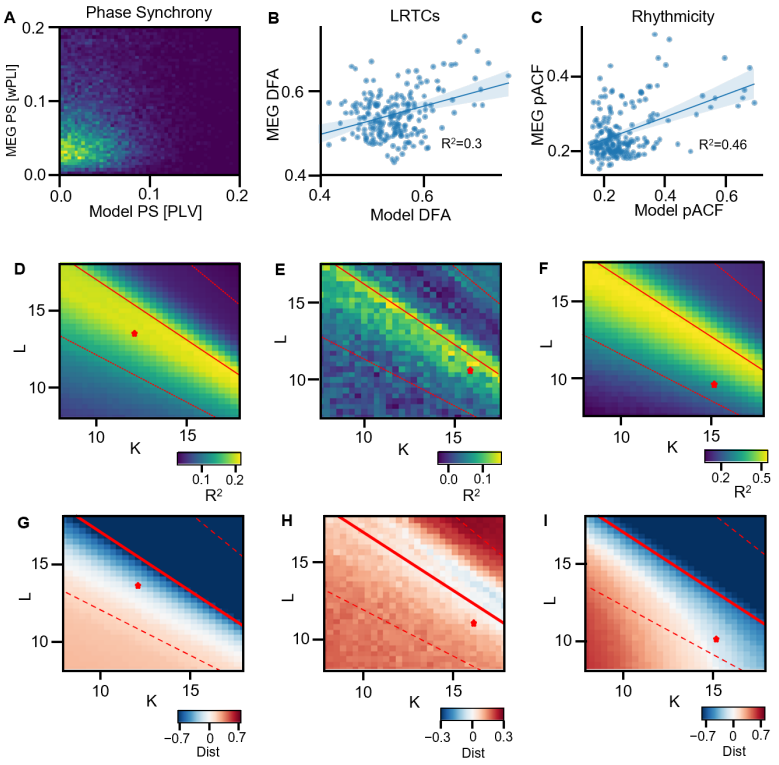

Figure 5. The model observables on the subcritical slope of the Griffiths Phase are the most similar to those found in MEG recordings. A, B, C The primary observables of oscillatory activity compared between real and model timeseries: Phase Synchrony (PS) operationalized with wPLI for MEG data and PLV for the model (**A**), LRTCs operationalized with DFA (**B**), and rhythmicity measured with pACF (**C**). **D, E, F** An average pearson correlation coefficient between the real and simulated PS (**D**), DFA (**E**), and pACF (**F**). **G,H,I** Kolmogorov-Smirnov distance measured between distributions of the real and simulated PS (**G**), DFA (**H**) and rhythmicity (**I**). Positive distance means that the real data observables tend to be higher than in the model and negative means that the model overshoots the physiological values. The red dots indicate location of the model observables and parameters used in **A,B,C**. Solid red lines indicate the median critical ridge, dashed lines indicate 5th and 95th percentiles of critical ridge slope and intercept estimated from an individual node-level positions (Supplementary Figure 2.A).

Brain dynamics is the most correlated with observables during the resting-state in subcritical region

The local synchrony and node order in the Hierarchical Kuramoto model can be operationalized using the phase locking of the node oscillators, which is bound between 0 and 1 by construction. But power does not directly measure the local synchronization – construct of rhythmicity, and the phase autocorrelation function (pACF), which measures phase stability, can be used to quantify oscillatory spectra ***Myrov et al.*** (***2024***). Next, as a system with multiple interacting units - nodes - their functional relationship can be quantified by phase synchronisation ***Lachaux et al.*** (***1999***) and moderate levels of phase synchronisation are a signature of healthy brain activity ***Palva et al.*** (***2005***). As a hallmark observable of brain criticality, neural oscillations exhibit scale-free long-range temporal correlations ***Palva et al.*** (***2013***), which are strongest at the critical point and can be operationalised with Detrended Functional Analysis (DFA) ***Linkenkaer-Hansen et al.*** (***2001a***).

To assess the similarity of observables of neural dynamics between the real MEG recordings and the simulated data, we initialised inter-node weights with a personalised mean-normed structural connectome and simulated time series with varying local and global control parameters. Then, to account for filter-induced spurious interactions, we filtered the real part of the simulated signal using the Morlet wavelet transform for 41 log-spaced frequencies (from 2 to 99 Hz, number of cycles = 5).

Next, we estimated model phase synchrony (PS) using PLV and wPLI in the MEG data (Figure 5A), criticality level using DFA (See Figure 5B), rhythmicity using pACF (See Figure 5C). To assess linear relationships between there metrics, we computed Pearson's correlation coefficient between observations from model nodes/edges and MEG parcels/edges belonging to the same anatomical zone. We also calculated the Kolmogorov-Smirnov test statistic to assess whether the distributions of the values were similar. To account for variability in the location of the critical ridge, we estimated confidence intervals of its position by pooling its slopes

and intercepts across all nodes, and calculated the median, 5th, and 95th percentiles and used them as lower and upper bounds (Supplementary Figure 2 A).

We found that the topological profiles of phase synchronisation are most similar between the real-data and model located in the subcritical slope of the extended critical zone, both in terms of correlation and distribution distances (See Figure 5D). The magnitude of phase-synchronization is undershot in the subcritical zone, while in the critical zone it exceeds the values observed in the real data (See Figure 5G). In addition, simulations with the most optimal Kolmogorov-Smirnov statistic (See Figure 5D) belong to a less critical region in contrast to the most optimal correlation.

DFA anatomy is best reconstructed following the critical ridge (See Figure 5E), and values in both subcritical and critical zones are lower than those observed in the MEG recordings (See Figure 5H), which supports the notion that the human brain operates primarily in a subcritical-critical zone. The rhythmicity properties follow a pattern similar to phase synchrony, with the highest correlation observed in a region just below the critical ridge (See Figure 5F), and the distributions of values are closest to those observed in the less critical region (See Figure 5I). Interestingly, the ridge with the lowest Kolmogorov-Smirnov distance for pACF is not linear as for PS and DFA but rather has a curve-like shape that decreases as the local control parameter K increases (See Figure 5I).

Fitting to predefined phenotypes

Although the model with data-driven distribution of inter-node weights was able to reproduce physiologically plausible behaviour, the correlation with individual observables remained quite low, especially for critical properties such as DFA. This can be attributed to the fact that the model behaviour is strongly dictated by its parameters (See Figure 3G-I), such as inter-node weights, while in the real data the structural connectome cannot explain the functional relations completely (***Messaritaki et al.*** (***2021***); ***Garcés et al.*** (***2015***)). This leads to the need for digital twins - personalised models of brain activity designed to reproduce an individual's brain dynamics.

In previous work, models have been fitted to a functional connectome by shifting an edge weight between two nodes according to the difference gradient between an actual and predicted connectome (***Deco et al.*** (***2019***)). This approach allows for the accurate reproduction of individual phase synchronisation profiles, but to date there have been no studies of simultaneous fitting to phase synchronisation and criticality dynamics. To address this issue, we developed an algorithm that works with both functional connectome and criticality properties to learn model parameters from data (Figure 6A). We applied the idea of gradient-based learning by approximating the DFA as a gaussian function of the local control parameter (See Figure 6B, see Methods for details).

To validate the algorithm, we first generated artificial phenotypes with known changes in the control parameters and fitted a model to them. We created a vector of phenotype coefficients by increasing or decreasing local and global control parameters in selected functional zones (See Figure 6C). Then, we ran a phenotype-based simulation, calculated the PLV and DFA observables and used them to fit the model with the pre-phenotyping control parameters (See Figure 6D).

We found that after fitting, the model is able to reproduce the altered dynamics with high similarity (Pearson correlation coefficient for DFA is ~ 0.7 and ~ 0.8 for PLV See Figure 6H) and requires about 15 iterations to converge to optimal parameters (See Figure 6E,F). The reconstructed profiles are not only close in the distribution of values, but also follow a similar anatomical pattern (See Figure 6G,H).

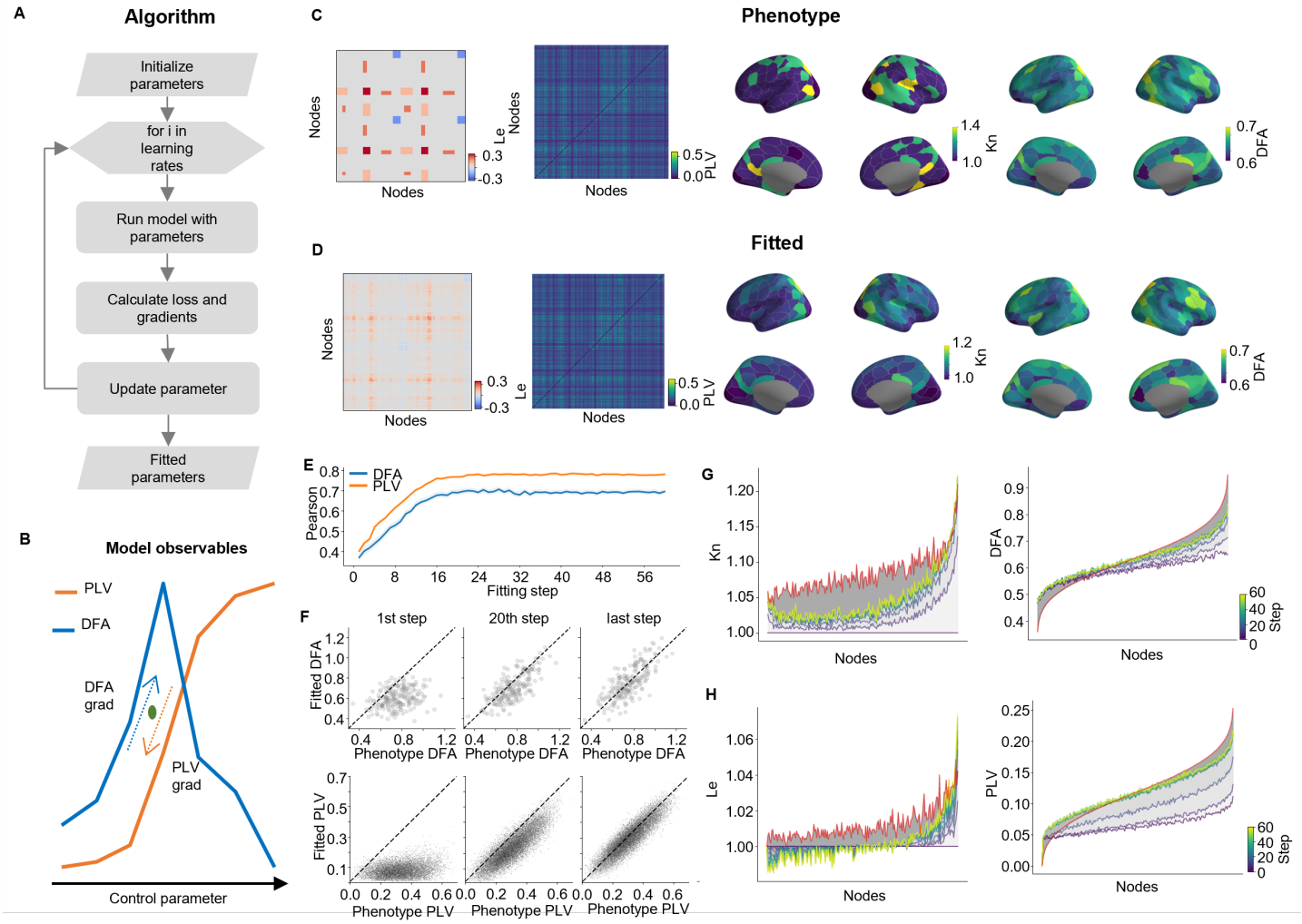

Figure 6. Fitting a model to predefined phenotypes. A A flowchart of the fitting algorithm. **B**. The concept of the gradient direction as a function of a control parameter. **C**. An artificial phenotype created by multiplying edge weights and local control parameters on a multiplier alongside with functional connectome matrix and DFA topography of a phenotype. **D**. Learned parameters of a model fitted to a predefined phenotype and its Functional Connectome and topography of the best-fit model. **E**. Pearson correlation coefficient between a phenotype and a model observables as a function of a fitting step. **F**. Scatterplots of a phenotype and a fitted model observables for different fitting steps. **G**. Learned coefficients for the local control parameter (left) and DFA (right) as a function of the fitting step. **H**. Learned coefficients for the edge weights (left) and PLV (right) as a function of the fitting step.

Personalized digital-twins of oscillatory neural dynamics

The actual level of neural dynamics observables depend of various individual physiological properties such as genetic polymorphism (***Simola et al.*** (***2022***)), cyto-architecture and transmitter density (***Siebenhühner et al.*** (***2024***)), excitation and inhibition gradient (***Wang*** (***2020***)) and balance ***Abeysuriya et al.*** (***2018***). However, some of those parameters could not be observed directly in the human-based experiments due to being to expensive or ethical limitations. In addition, phenomenological models may not have clear physiological comparison of parameters (such as local coupling in the hierarchical Kuramoto model) to physiological measurements and can only be mapped indirectly. Therefore, it may not be possible to create precise models per-se using only the prior knowledge and any model has to be adjusted to reproduce individual properties.

The idea of computational models tailored to reproduce a personalized model dynamics aka *digital twins* has been a rising research topic in recent years ***San*** (***2021***) especially in application to health studies and medicine ***Laubenbacher et al.*** (***2024***); ***Katsoulakis et al.*** (***2024***), in application to the neuroscience field, a Digital Twin Brain is a system that can reproduce individual neural dynamics. The critical brain hypothesis implies that a critical state-space emerges from the underlying parameters and is a basis for an individual

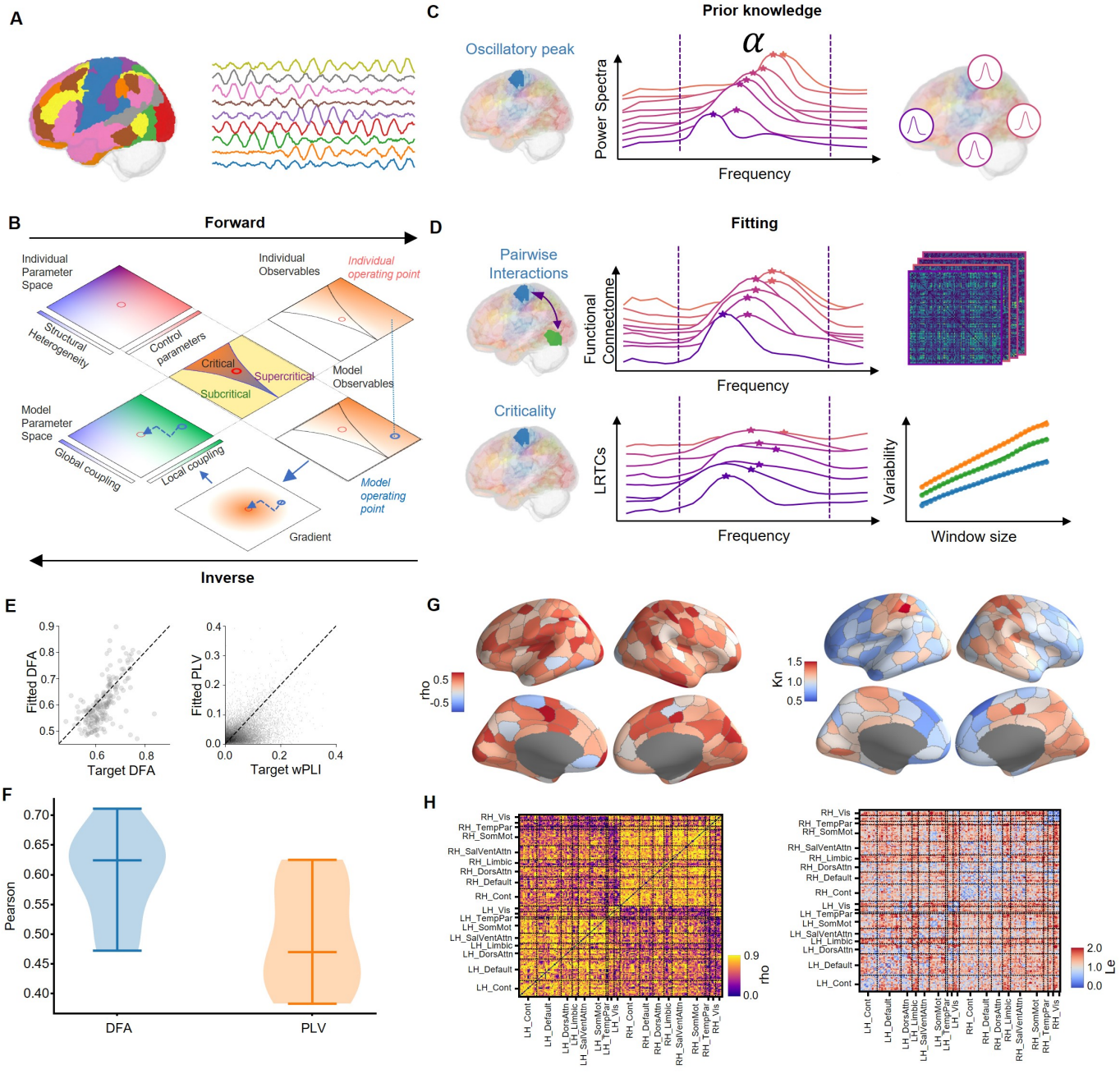

Figure 7. The concept of a Digital Twin Brain. A given Resting-State MEG recordings of a single subject (**A**) are used to extract the oscillatory peaks in the alpha frequency and set central frequencies of each node (**B**). The critical brain hypothesis implies that a critical state-space emerges from the underlying parameters and is a basis for an individual operating point reflected in observables. A Digital Twin Brain shares the same critical space with a real system and the gradient of differences between the model and the target observables can be used to adjust the model parameters (**C**). **D** The metric of pairwise interactions measured with phase synchrony and the DFA exponent are extracted from the MEG recordings and are used to fit the model. **E** Scatterplots of DFA exponents and phase synchrony for a single-subject best fit model. **F** Violinplots for distributions of the Pearson correlation coefficient for best-fit models across the MEG cohort. **G** Topography of correlation coefficients between the best-fit model and target DFA (left) and an average learned local control parameter (Kn, right). **H** Correlation coefficient between the best-fit model and target PS (left) and an average learned global control parameter (right, Le)

operating point reflected in observables (Figure 7A). A Digital Twin Brain shares the same critical space with a real system but the model individual operating point may be different due to non-perfect parameters and model assumptions. To negate this effect a model parameters and thus the position in the critical space may be adjust by following the gradient of different between a model

and a target observables (See Figure 7B).

To match the structure of a personal connectivity architecture, the initial edge weights were initialised with a mean-normed structural connectome obtained from the subject DWI data (See Figure 1A). We also derived the peak alpha frequency from an individual PSD spectrum and used it as an average value for Gaussian distribution of oscillator frequencies (See Figure 7C).

The phase synchronization and criticality are fundamental observables in the critical brain hypothesis and their alterations are associated with cognitive states, physiological changes, and mental disorders, so it is natural that a digital twin brain would be able to reproduce such properties of an individual. To create a DTB of a participant, we computed average wPLI as a function of frequency and used a wPLI functional connectome at the peak in alpha frequency and DFA values at the same frequency as a fitting target (See Figure 7D).

We discovered that the fitted model successfully replicates individual critical dynamics within both the physiologically plausible range of values and the topographical correlations (See Figure 7E). On the cohort level, we found that the Pearson correlation coefficient between the best-fit model and an individual recordings are higher for DFA that were observed for PS (average 0.63 for DFA and 0.47 for PLV, See Figure 7F). We also found that the fitting quality is positively correlated with the fraction of significant values (Supplementary Figure 3), we assume that the non-significant values are dictated by the noise which is not possible to fit.

As the next step we assessed reconstruction quality for each node and edge individually by computing the correlation between predicted and an real-data DFA exponents (for single nodes) and phase synchrony (for edges). While checking the fitted weights of a model we mean-normalized them by dividing all the weights on the average weight for each subject to take into account an individual bias.

For DFA exponents, we found that the visual and temporal areas yield the highest correlation simultaneously with the highest weights for local control parameter on average (See Figure 7G), while the default subsystem has the worst predictions and the lowest weights. As for PLV, at first glance, the inter-hemi connections are poorly reconstructed in contrast with intra-hemi (average correlation is 0.51 for connections between hemispheres and 0.64 for connections inside a hemisphere, See Figure 7H). At second glance, we found that the visual subsystem remains an outlier where PS between it and other subsystems was fit with low quality but within it nodes the correlation remains high. Interestingly, the edge weights between nodes that belong to the same subsystem tend to be lower in contrast to the edges connecting different subsystem (0.93 for intra-nodal connectivity and 1.23 for inter-nodal, See Figure 7H).

Discussion

Neuronal oscillations in the human brain exhibit high variability across many observables such as power, synchronization, and rhythmicity. Notably, they also display long-range temporal correlations (LRTCs) and avalanche dynamics, which are key signatures of critical-like behaviour (***Linkenkaer-Hansen et al.*** (***2001b***); ***Beggs and Plenz*** (***2003***)). The hypothesis of the 'critical brain' suggests the brain operates near a phase transition between order and disorder. However, there is not an abundance of large-scale models of oscillatory synchronization with the ability to capture in-vivo-like critical synchronization dynamics observed with electrophysiological neuroimaging.

We introduced here a hierarchical whole-brain-scale Kuramoto model where interconnected nodes–corresponding to parcels of a cortical atlas–were represented with large populations of oscillators (See Figure 1). This approach yields realistic-like oscillatory synchronization dynamics with critical properties governed by the local and inter-areal coupling control parameters. Hierarchical Kuramoto model maps well to human neuroimaging data because each parcel maps to a single node that in itself is capable of producing several features of critical meso-scale brain dynamics such as LRTCs, power spectrum, phase synchrony, and rhythmicity (***Fuscà et al.*** (***2023***); ***Arnulfo et al.*** (***2020***); ***Wang et al.*** (***2023b***); ***Myrov et al.*** (***2024***)).

The model reproduced the expected phase transition so that inter-areal phase synchronization and local order were low in the subcritical phase and became fully synchronized in the supercritical phase(***Dorfler and Bullo*** (***2011***); ***Fuscà et al.*** (***2023***)). We also found the model to exhibit an extended, Griffiths-phase-like, critical regime when using a realistic structural connectome (***Muñoz*** (***2018***); ***Villegas et al.*** (***2014***); ***Fuscà et al.*** (***2023***)).

Importantly, inter-areal amplitude correlations at the level of whole-brain networks, *i.e.*, correlations between the node order time series, peaked at criticality and were low in both sub- and supercritical phases. This is in line with the notion of criticality maximazing

dynamic correlation (***Beggs*** (***2007***)) and has been found earlier in a system with two inter-connected spiking networks (***Avramiea et al.*** (***2022***)).

Analyzing the structure-function relationships in the model, we found that the shape of linear correlations between model's structural connectivity and observables of oscillatory dynamics was dictated by the model's operating point. Node order had the strongest correlation with the local control parameter (K) and PLV the strongest correlation with the global control parameter (L) in the subcritical region. This linear structure-function relationship broke down at criticality. On the other hand, the correlation of inter-areal amplitude correlations with structural connectivity peaked at criticality and vanished in both sub- and super-critical phases.

The alignment of observables between model and neuroimaging data is a prerequisite for assessing the physiological plausibility of whole-brain models. We first compared the model against resting-state MEG data by using the power spectrum. To reproduce the power spectrum of a recording, we initialized the distribution of oscillator frequencies to match the shape of the power spectrum of each node without the $\frac{1}{f}$ component.

We found that the model is able to reproduce the spectral characteristics with the highest reliability around the subcritical side of the extended critical regime with high local and low global control parameters. Varying these parameters changes the rhythmic properties from an almost complete absence of oscillations in the subcritical region to strong, sustained oscillations with peak shifted towards weighted average of the oscillator frequencies.

Next, we investigated similarity between model and real data for bivariate interactions assessed by phase synchrony, for LRTCs assessed with the Detrended Fluctuation Analysis (DFA) exponent, and for rhythmicity assessed by the phase autocorrelation function. We created a model with an inter-node weight matrix obtained from individual diffusion tensor imaging (DWI) to match the physiological nature of the structural connectome. Comparing the model dynamics observables with the real data, we found that the most physiologically plausible model dynamics were observed within the subcritical side of the extended critical regime. We also found that the shape of the most physiologically plausible region for PLV and DFA follows linear shape as a function of control parameters, unlike rhythmicity, while having the same linear correlation ridge, has a curved shape for similarity of distributions. Overall, the model exhibit highest resemblance with high local coupling (K) and low global (L) for most of the observables.

Although the distributions of modelled properties of oscillatory activity were similar to those in real data, the linear correlations between them remained low, especially for DFA exponents. This might result from low correlations between structural and functional connectivity in real data which contradicts the observed model behaviour, implying that the development of precise models requires a personalized approach to restore the unknown underlying parameters. In prior-art, the process of fitting the model with experimental data has, e.g., been implemented by using the Bayesian approach (***Williams et al.*** (***2023***); ***Oesterle et al.*** (***2020***)). This, however, is computationally intensive and has limited applicability when the number of parameters exceeds hundreds or thousands of values. However, when a model is known, one can apply model-specific methods such as fitting to time-resolved connectome (***Kringelbach et al.*** (***2020***)) or adaptation of the gradient descent approach to fit the control parameters, such as the pairwise edge weights between all model nodes (***Deco et al.*** (***2019***)). This approach allows to avoid exhaustive search through the model parameter space and converges typically just in some tens of iterations.

In this work, we extended the gradient-descent fitting oscillatory models by taking into account both criticality and synchronization properties. We validated the approach on simulated data by creating an artificial phenotype via increasing or decreasing model control parameters on predefined value and found that this method allows to reconstruct the phenotype with both high correlation of observables such as DFA exponent and PLV and the restored control parameters are similar and follow the same anatomical pattern as phenotype.

In conclusion, we introduce here a framework for generative hierarchical models of synchronization dynamics that enable explicit representation of local and inter-areal coupling and observations of emergent multi-scale synchronization dynamics. Our results show that the Hierarchical Kuramoto model produces meso- and macro-scale synchronization-dynamics observables that are physiologically plausible in the light of, e.g., magneto- and electroencephalography (M/EEG) data. We further advance here a model fitting with individual experimental data that uses not only functional connectivity but also critical dynamics to converge model parameters that are personalized with individual multimodal data e.g. M/EEG and structural-connectivity.

Methods and Materials

Hierachical kuramoto model

In the classical Kuramoto model, a population is defined as multiple oscillators with all-to-all coupling mediated by a sinusoidal interaction function with a given frequency for each oscillator

$$\frac{\delta\phi_i}{\delta t} = \omega_i + \frac{1}{N}\sum_{j=1}^{N} K_{ij} sin(\phi_j - \phi_i)$$

where N is a total number of oscillators, ϕ_i is an i-th oscillator phase, ω_i is the frequency of i-th oscillator and K_{ij} is the coupling parameter between i-th and j-th oscillators.

However, the model represents basic dynamics and for the final analysis, data is often aggregated across all oscillators e.g. by computing a model order defined as the absolute value of the average oscillator phase. This approach makes comparison with real brain imaging data a challenging task. To overcome this we introduce a hierarchical extension of the Kuramoto model with multiple nodes where each node may correspond to a recording from a single brain area or electrode.

Each node consists of multiple oscillators and the behavior of each oscillator could be explained in three components:

$$\frac{\delta\phi_i^n}{\delta t} = Natural + Internal + External + Noise$$

Where $Natural = w_i^n$ or the center frequency of an i-th oscillator in n-th node and ϕ_i^n is the phase of i-th oscillator in n-th node,

$$Internal = \frac{K_n}{N}\sum_{j=1}^{N} sin(\phi_i^n - \phi_j^n)$$

where K_n is a local coupling parameter of the n-th node and N is a total number of oscillators within the node. In this context, the phase of each oscillator is shifted towards the average phase difference with oscillators in the same node,

$$External = \sum_{j=1}^{k} L_{n,j} * W_{n,j} * sin(\phi_i^n - \Phi_j) * R_j$$

Where $L_{n,j}$ is a coupling coefficient between n-th and j-th nodes (global control parameter), $W_{n,j}$ is a structural connectivity between n-th and j-th nodes, Φ_j is a cyclic average of the phases the average of the n-th node defined as $\Phi_j = arg(\frac{1}{N}\sum_{q=1}^{N} e^{i\phi_q^j})$ and R_j is an order of j-th node (see the definition below). In this term the phase of each oscillator is compared to the average phase of other nodes and weighted by a node order and structural connectivity.

and $Noise = \eta_i^n$ is a gaussian white noise for i-th oscillator in n-th node.

At the final step, we aggregated the signal for each node by averaging complex values of all oscillators and the analytical signal of n-th node is defined as $S_n = \frac{1}{N}\sum_j = 1^N e^{i*\phi_j^n}$. Thus, one is able to match a model's node to a single brain area or any other source of LFP recordings.

To improve computational performance we use complex-value representation for oscillator states. Thus, the coupling function between oscillators x and y becomes $imag(x * y^*)$ where x, y are complex values representating an oscillator phase and y^* is a conjugate of y.

Observables of oscillatory dynamics

One of the fundamental observables of the Kuramoto model is its order – indexing the oscillators' synchrony inside each node – defined as an absolute value of an average complex-valued phase across oscillators that belong to the same node

$$R = |\frac{1}{N}\sum_{i=1}^{N} e^{i*\theta_i}|$$

Where N is the number of oscillators and θ_i is the phase of the i-th oscillator.

To estimate inter-areal phase interactions we computed Phase Synchrony metrics for each pair of nodes (model data) or parcels (MEG). For the model, we used the phase locking value (PLV) defined as absolute value of complex PLV

$$cPLV = E[CS_{x,y}]$$

Where E[.] denotes the expected value and $CS_{x,y}$ denotes the cross-spectrum between a complex signals X and Y. In practice, cPLV is estimated using limited data and sample cPLV is defined as

$$\overline{cPLV}_{sample} = \frac{1}{N}\sum_{i=1}^{N} CS_{x,y}$$

where N is the total number of samples.

For MEG data we used the weighted Phase Lag Index (wPLI) which is insensitive to spurious zero-lag interactions and defined as:

$$wPLI = \frac{|\sum_{i=0}^{N} imag(CS_{x,y})|}{\sum_{i=0}^{N} |imag(CS_{x,y})|}$$

where $imag(CS_{x,y})$ is the imaginary part of the cross-spectrum of the complex time series x and y ***Wang et al.*** (***2018***); ***Vinck et al.*** (***2011***).

To measure long-range temporal correlations (LRTCs) in a model and MEG recordings, we used the Detrended Fluctuations analysis (DFA, ***Hardstone et al.*** (***2012***)), which in order to speed up the estimation we computed in the Fourier domain ***Nolte et al.*** (***2019***). To obtain the DFA exponents from model or MEG data, the fluctuations as a function of window sizes were fitted with a robust linear regression (***Huber*** (***1973***)) with a bisquare weight function.

To estimate rhythmicity of oscillations we applied the Phase Autocorrelation Function (pACF, ***Myrov et al.*** (***2024***)). Typically, pACF assesses the lifetime of oscillations by checking whether the time-lagged PLV crosses a threshold. However, super-critical models yield stable oscillations with lifetime $\to \infty$. Therefore, we estimated rhythmicity as an average pACF across lags of $1...5$ cycles which ensures that the value is bound in $[0; 1]$.

Data acquisition

Fifteen minutes eyes-open resting-state data were recorded from 20 healthy controls with 306-channel MEG (TRIUX, MEGIN Oy, Helsinki, Finland; 204 planar gradiometers and 102 magnetometers) at BioMag Laboratory, HUS Medical Imaging Center, Helsinki, Finland and 306-channel MEG (TRIUX neo, MEGIN Oy, Helsinki, Finland; 204 planar gradiometers and 102 magnetometers) at MEG Core, Aalto University, Espoo, Finland. Bipolar horizontal and vertical electrooculography (EOG) and electrocardiography (ECG) were also recorded. Participants were instructed to seat in a dimly lit room and keep their eyes open to focus on a cross displayed at the center of a screen in front.

T1-weighted anatomical magnetic resonance imaging (MRI) and diffusion weighted imaging (DWI) scans were obtained with a 3 Tesla whole-body MRI scanner (Magnetom Skyra, Siemens, Munich, Germany) at AMI Centre, Aalto University using a 32-channel head coil. T1-weighted MRI data were recorded with a resolution of 0.8×0.8×0.8 mm, repetition time of 2530 ms, and echo time of 3.42 ms. DWI data were recorded with a resolution of 3.0×3.0×3.0 mm, repetition time of 4100 ms, and echo time of 105 ms.

The study protocol for MEG, MRI, and DWI data was approved by the HUS ethical committee (**HUS/3043/2021**, 27.4.2022), written informed consent was obtained from each participant prior to the experiment, and all research was carried out according to the Declaration of Helsinki.

MEG data preprocessing and source modeling

The MNE software (https://mne.tools/stable/index.html) was used for data preprocessing and source modeling. Temporal signal space separation (tSSS) in the Maxfilter software (Elekta Neuromag Ltd., Finland) was used to suppress extracranial noise from MEG sensors, interpolate bad channels, and compensate for head motions. Independent components analysis was used to identify and remove components that were correlated with ocular (using the EOG signal), heart-beat (using the magnetometer signal as reference), or muscle artefacts.

We used the FreeSurfer 7.3.2 software (https://surfer.nmr.mgh.harvard.edu/) for volumetric segmentation of MRI data, surface reconstruction, flattening, and cortical parcellation. Source reconstruction was performed with minimum norm estimation (MNE) using dynamic statistical parametric maps (dSPM). A surface-based source space with 5 mm spacing and 1 layer (inner skull) symmetric boundary element method (BEM) was used in computing the forward operator, and noise covariance matrices was obtained from preprocessed data filted to 151-249 Hz. We then estimated vertex fidelity to obtain fidelity-weighted inverse operators to reduce the effects of spurious connections resulting from source leakage and collapsed the inverse-transformed source time series into parcel time series in a manner that maximizes the source-reconstruction accuracy (***Korhonen et al.*** (***2014***); ***Siebenhühner et al.*** (***2020b***)). Source time series were collapsed to the 200 parcels of the Schaefer atlas (***Schaefer et al.*** (***2018***)).

In this study, we used complex Morlet wavelets to obtain a narrow-band representation of a MEG signal (***Cohen*** (***2019***)). 50 Hz line-noise and it's harmonics were suppressed with a notch filter with 1 Hz band transition widths. The band-pass (1-249 Hz) filtered data were then separated into narrow frequency bands with 41 equally log-spaced Morlet wavelets with frequencies ranging from 1 Hz to 100 Hz (number of cycles in a Morlet Wavelet = 5.0).

DWI data preprocessing

The DWI data preprocessing, including denoising and motion correction, was conducted using the MRtrix3 3.0.1 Toolbox (***Tournier et al.*** (***2019***)) and FMRIB Software Library (FSL) 6.0.5 (***Jenkinson et al.*** (***2012***)). To lessen potential biases or artifacts arising during image acquisition or processing, the Advanced Normalization Tools (ANTs) 2.3.5 was used (***Avants et al.*** (***2009***)). For T1-weighted anatomical MRI data preprocessing, creation of head models and cortical surface reconstruction, we used the open-source FreeSurfer 7.3.2 software (available at https://surfer.nmr.mgh.harvard.edu/, ***Fischl*** (***2012***)). In the subsequent step, Constrained Spherical Deconvolution (CSD) (***Tournier et al.*** (***2007***)) was employed to determine the fiber orientation distributions (FODs) within each voxel, allowing for the accurate decomposition of the diffusion signal into individual fiber orientations. In order to improve the accuracy of fiber tracking, anatomically-constrained tractography (ACT, ***Smith et al.*** (***2012***)) was also applied by incorporating anatomical information through the five-tissue-type (5TT) segmentation derived from diverse brain tissues. The resulting FODs provided a detailed map of white matter tracts. For tractography construction the principal diffusion direction was obtained from each of the 20 000 000 seed points. To refine the quality of the diffusion image and minimize tractogram reconstruction biases, we applied the Spherical informed filtering of tractograms approach (SIFT2, ***Smith et al.*** (***2013***)).

T1-weighted anatomical MRI and DWI coregistration was performed using the Spm 12 package within MATLAB R2022a software. All preprocessing steps were executed on the CentOS Linux operating system, operating on the Triton high-performance computing cluster at Aalto University.

Following preprocessing, structural connectomes (SCs) were constructed as edge-adjacency matrices representing the count of white matter connections between parcelled cortical and subcortical brain regions. The resulting matrices are symmetric, reflecting undirected pairwise connections between brain regions (nodes). The nodes correspond to the 200 parcels of the Schaefer atlas (***Schaefer et al.*** (***2018***)), matched with Yeo 17 networks (***Yeo et al.*** (***2011***)).

Model fitting

The dependency of PLV over parameters was defined as a sigmoid function ($S(P)$) since PLV shows monotonically increasing behavior. This, the gradient of edge weights matrix is equal to the difference between simulated and a target functional connectome matrix, while the sign of difference shows the direction of the gradient as well (See Figure 6B).

$$grad = [S(P) * (1 - S(P))] * loss \tag{1}$$

Where S is a sigmoid function, P its parameter (e.g. global or local control parameter) and loss is the difference between target and model FC.

The critical state is characterized by peak in the DFA as a function of control parameter (K, See Figure 6B), therefore it is possible to approximate this dependency using the gaussian function ($g(P)$) and use its derivative for a gradient decent-based fitting as shown in the equation 2.

$$grad = -\frac{P}{\sigma^2} * g(P) * loss \tag{2}$$

where parameters of the gaussian function ($g(P)$): σ and μ equal to 0.5 and 1, respectively.

We applied the multiobjective steepest descent method (***Liu and Reynolds*** (***2016***)) to integrate gradients from various objective functions and we used sum of normalized gradients if they have same direction. Following the approach from ***Liu and Reynolds*** (***2016***), we determined the Pareto optimal solution in case where gradients exhibited divergent directions:

$$G = (\frac{||g_2||^2 - g_1^T g_2}{||g_1||^2 - g_1^T g_2} * -g_1) - g_2 \tag{3}$$

Local control parameter affects both criticality and phase synchrony properties and following this observation, we computed the gradients for K fitting as a sum of DFA and PLV gradients. Because DFA function is not a monotonically growing, we used a sign of the PLV gradient:

$$G_K \leftarrow sign(grad_{kPLV}) * abs(\frac{grad_{kDFA}}{||g_1||^2||grad_{kDFA}||} + \frac{grad_{kPLV}}{||g_1||^2||grad_{kPLV}||}) \tag{4}$$

We applied L1 regularization with $\lambda = 0.0001$ to avoid overfitting and enforce model weight sparsity.

We incorporated the Root Mean Square Propagation (RMSprop) strategy for the adaptive learning rate:

$$grad_i = \beta * grad_{i-1} + (1 - \beta) * grad_i^2 \tag{5}$$

Where $\beta = 0.9$ and represents the default value for the moving average coefficient, $grad_i$ is a gradient value at step i.

And control parameters were updated following the next equation 6:

$$P = P - \frac{lr * grad}{\sqrt{grad^2}} \tag{6}$$

where P is either a local or global control parameter, lr is a learning rate, $grad$ is a gradient for the parameter.

Combining all of these steps, the final fitting follows the next algorithm:

Algorithm 1 Fitting algorithm

Require: $target_{DFA}, targetl_{wPLI}$
Ensure: $weights, K_n$

function fitting(target)
  $G_{Ksquared} \leftarrow 0$
  $G_{wsquared} \leftarrow 0$
  $weights \leftarrow 1$
  $K_n \leftarrow 1$
  for $lr \leftarrow 1$ to N **do**
    $loss_{PLV} \leftarrow model_{PLV} - target_{wPLI}$
    $loss_{DFA} \leftarrow model_{DFA} - target_{DFA}$
    $grad_{kPLV} \leftarrow [S(K) * (1 - S(K))] * loss_{PLV}$
    $grad_{kDFA} \leftarrow -K_n/\sigma^2 * loss_{DFA} * g(K_n)$
    $grad_{wPLV} \leftarrow [S(weights) * (1 - S(weights))] * loss_{PLV}$
    $grad_{wDFA} \leftarrow -weights/\sigma^2 * loss_{DFA} * g(weights)$
    if $grad_{wPLV}^T * (grad_{wPLV} - grad_{wDFA})) > 0$ **then**
      $G_w \leftarrow (\frac{||grad_{wDFA}||^2 - grad_{wPLV}^T * grad_{wDFA}}{||grad_{wPLV}||^2 - grad_{wPLV}^T * grad_{wDFA}} * -grad_{wPLV}) - grad_{wDFA}$
      $G_w \leftarrow -G_w/||G_w||$
    else
      $G_w \leftarrow grad_{wPLV}/||grad_{wPLV}|| + grad_{wDFA}/||grad_{wDFA}||$
    end if
    $G_K \leftarrow sign(grad_{kPLV}) * abs(grad_{kDFA}/||grad_{kDFA}|| + grad_{kPLV}/||grad_{kPLV}||)$
    $G_{Ksquared} \leftarrow 0.9 * G_{Ksquared} + 0.1 * G_K^2$
    $G_{wsquared} \leftarrow 0.9 * G_{wsquared} + 0.1 * G_w^2$
    $weights = weights - lr * G_w/\sqrt{G_{wsquared}}$
    $K_n = K_n - lr * G_K/\sqrt{G_{Ksquared}}$
  end for
  return $weights, K_n$
end function

Data availability

Raw data cannot be made available due to data privacy regulations set by the ethical committees. The data underlying results to reproduce the main findings will be deposited in a suitable repository prior to the publication. Other types of data can be shared upon reasonable request.

Code availability

The model code will be open-sourced after the publication. The implementation of model fitting and code to reproduce this study results will also be published in a suitable repository prior to the publication.

Ethics

All participants provided written informed consent for their data to be used, and all studies were approved by the institutional review boards at the respective institutions.

Declaration of Competing Interests

The authors declare no competing interests.

Acknowledgements

We thank Sheng Wang, Felix Siebenhühner and Joonas J. Juvonen for feedback about the study. We also thank professor Guido Nolte on helpful comments on an earlier version of the manuscript.

This study was supported by the Academy of Finland (J.M.P., project numbers: 296304), by the Juselius Foundation (S.P and J.M.P project number 240156).

Author Contributions

V.M. and J.M.P. conceived the study; V.M. wrote the model code; A.S. implemented the fitting algorithm; V.M. and A.S. wrote the analysis code; W.L. provided preprocessed MEG data; S.K. provided preprocessed DWI data; P.P. and M.V. recorded MRI and MEG data; All authors contributed to the writing of the manuscript. All authors read and approved the manuscript.

References

Abeysuriya RG, Hadida J, Sotiropoulos SN, Jbabdi S, Becker R, Hunt BAE, Brookes MJ, Woolrich MW. A biophysical model of dynamic balancing of excitation and inhibition in fast oscillatory large-scale networks. PLOS Computational Biology. 2018 Feb; 14(2):e1006007. http://dx.doi.org/10.1371/journal.pcbi.1006007, doi: 10.1371/journal.pcbi.1006007.

Aburn MJ, Holmes CA, Roberts JA, Boonstra TW, Breakspear M. Critical Fluctuations in Cortical Models Near Instability. Frontiers in Physiology. 2012; 3. http://dx.doi.org/10.3389/fphys.2012.00331, doi: 10.3389/fphys.2012.00331.

Alamian G, Hincapié AS, Combrisson E, Thiery T, Martel V, Althukov D, Jerbi K. Alterations of Intrinsic Brain Connectivity Patterns in Depression and Bipolar Disorders: A Critical Assessment of Magnetoencephalography-Based Evidence. Frontiers in Psychiatry. 2017 Mar; 8. http://dx.doi.org/10.3389/fpsyt.2017.00041, doi: 10.3389/fpsyt.2017.00041.

Arnulfo G, Wang SH, Myrov V, Toselli B, Hirvonen J, Fato MM, Nobili L, Cardinale F, Rubino A, Zhigalov A, Palva S, Palva JM. Long-range phase synchronization of high-frequency oscillations in human cortex. Nature Communications. 2020 Oct; 11(1). http://dx.doi.org/10.1038/s41467-020-18975-8, doi: 10.1038/s41467-020-18975-8.

Avants BB, Tustison N, Song G, et al. Advanced normalization tools (ANTS). Insight j. 2009; 2(365):1–35.

Avramiea AE, Masood A, Mansvelder HD, Linkenkaer-Hansen K. Long-range amplitude coupling is optimized for brain networks that function at criticality. Journal of Neuroscience. 2022; 42(11):2221–2233.

Beggs JM. The criticality hypothesis: how local cortical networks might optimize information processing. Philosophical Transactions of the Royal Society A: Mathematical, Physical and Engineering Sciences. 2007 Aug; 366(1864):329–343. http://dx.doi.org/10.1098/rsta.2007.2092, doi: 10.1098/rsta.2007.2092.

Beggs JM, Plenz D. Neuronal Avalanches in Neocortical Circuits. The Journal of Neuroscience. 2003 Dec; 23(35):11167–11177. http://dx.doi.org/10.1523/JNEUROSCI.23-35-11167.2003, doi: 10.1523/jneurosci.23-35-11167.2003.

Boon LI, Geraedts VJ, Hillebrand A, Tannemaat MR, Contarino MF, Stam CJ, Berendse HW. A systematic review of MEG-based studies in Parkinson's disease: The motor system and beyond. Human Brain Mapping. 2019 Mar; 40(9):2827–2848. http://dx.doi.org/10.1002/hbm.24562, doi: 10.1002/hbm.24562.

Breakspear M, Heitmann S, Daffertshofer A. Generative models of cortical oscillations: neurobiological implications of the Kuramoto model. Frontiers in human neuroscience. 2010; 4:190.

Brookes MJ, Woolrich M, Luckhoo H, Price D, Hale JR, Stephenson MC, Barnes GR, Smith SM, Morris PG. Investigating the electrophysiological basis of resting state networks using magnetoencephalography. Proceedings of the National Academy of Sciences. 2011 Sep; 108(40):16783–16788. http://dx.doi.org/10.1073/pnas.1112685108, doi: 10.1073/pnas.1112685108.

Buzsáki G. Rhythms of the Brain. Oxford University Press; 2006. https://doi.org/10.1093/acprof:oso/9780195301069.001.0001, doi: 10.1093/acprof:oso/9780195301069.001.0001.

Buzsáki G, Anastassiou CA, Koch C. The origin of extracellular fields and currents–EEG, ECoG, LFP and spikes. Nat Rev Neurosci. 2012 May; 13(6):407–420.

Cabral J, Castaldo F, Vohryzek J, Litvak V, Bick C, Lambiotte R, Friston K, Kringelbach ML, Deco G. Metastable oscillatory modes emerge from synchronization in the brain spacetime connectome. Communications Physics. 2022 Jul; 5(1). http://dx.doi.org/10.1038/s42005-022-00950-y, doi: 10.1038/s42005-022-00950-y.

Castaldo F, Páscoa dos Santos F, Timms RC, Cabral J, Vohryzek J, Deco G, Woolrich M, Friston K, Verschure P, Litvak V. Multi-modal and multi-model interrogation of large-scale functional brain networks. NeuroImage. 2023 Aug; 277:120236. http://dx.doi.org/10.1016/j.neuroimage.2023.120236, doi: 10.1016/j.neuroimage.2023.120236.

Chialvo DR. Emergent complex neural dynamics. Nature Physics. 2010 Oct; 6(10):744–750. http://dx.doi.org/10.1038/nphys1803, doi: 10.1038/nphys1803.

Cohen MX. A better way to define and describe Morlet wavelets for time-frequency analysis. NeuroImage. 2019 Oct; 199:81–86. https://doi.org/10.1016/j.neuroimage.2019.05.048, doi: 10.1016/j.neuroimage.2019.05.048.

Cowan JD, Neuman J, van Drongelen W. Wilson–Cowan Equations for Neocortical Dynamics. The Journal of Mathematical Neuroscience. 2016 Jan; 6(1). http://dx.doi.org/10.1186/s13408-015-0034-5, doi: 10.1186/s13408-015-0034-5.

Dalla Porta L, Copelli M. Modeling neuronal avalanches and long-range temporal correlations at the emergence of collective oscillations: Continuously varying exponents mimic M/EEG results. PLOS Computational Biology. 2019 Apr; 15(4):e1006924. http://dx.doi.org/10.1371/journal.pcbi.1006924, doi: 10.1371/journal.pcbi.1006924.

David O, Friston KJ. A neural mass model for MEG/EEG:. NeuroImage. 2003 Nov; 20(3):1743–1755. http://dx.doi.org/10.1016/j.neuroimage.2003.07.015, doi: 10.1016/j.neuroimage.2003.07.015.

Deco G, Cruzat J, Cabral J, Tagliazucchi E, Laufs H, Logothetis NK, Kringelbach ML. Awakening: Predicting external stimulation to force transitions between different brain states. Proceedings of the National Academy of Sciences. 2019 Aug; 116(36):18088–18097. http://dx.doi.org/10.1073/pnas.1905534116, doi: 10.1073/pnas.1905534116.

Deco G, Kringelbach ML, Jirsa VK, Ritter P. The dynamics of resting fluctuations in the brain: metastability and its dynamical cortical core. Scientific Reports. 2017 Jun; 7(1). http://dx.doi.org/10.1038/s41598-017-03073-5, doi: 10.1038/s41598-017-03073-5.

Deco G, Ponce-Alvarez A, Mantini D, Romani GL, Hagmann P, Corbetta M. Resting-state functional connectivity emerges from structurally and dynamically shaped slow linear fluctuations. Journal of Neuroscience. 2013; 33(27):11239–11252.

Deco G, Sanz Perl Y, Vuust P, Tagliazucchi E, Kennedy H, Kringelbach ML. Rare long-range cortical connections enhance human information processing. Curr Biol. 2021 Oct; 31(20):4436–4448.e5.

Donoghue T, Haller M, Peterson EJ, Varma P, Sebastian P, Gao R, Noto T, Lara AH, Wallis JD, Knight RT, Shestyuk A, Voytek B. Parameterizing neural power spectra into periodic and aperiodic components. Nature Neuroscience. 2020 Nov; 23(12):1655–1665. http://dx.doi.org/10.1038/s41593-020-00744-x, doi: 10.1038/s41593-020-00744-x.

Dorfler F, Bullo F, On the Critical Coupling for Kuramoto Oscillators; 2011.

Fischl B. FreeSurfer. NeuroImage. 2012 Aug; 62(2):774–781. http://dx.doi.org/10.1016/j.neuroimage.2012.01.021, doi: 10.1016/j.neuroimage.2012.01.021.

Fries P. Rhythms for Cognition: Communication through Coherence. Neuron. 2015 Oct; 88(1):220–235. https://doi.org/10.1016/j.neuron.2015.09.034, doi: 10.1016/j.neuron.2015.09.034.

Fuscà M, Siebenhühner F, Wang SH, Myrov V, Arnulfo G, Nobili L, Palva JM, Palva S. Brain criticality predicts individual levels of inter-areal synchronization in human electrophysiological data. Nature Communications. 2023 Aug; 14(1). http://dx.doi.org/10.1038/s41467-023-40056-9, doi: 10.1038/s41467-023-40056-9.

Garcés P, Pereda E, Hernández-Tamames JA, Del-Pozo F, Maestú F, Ángel Pineda-Pardo J. Multimodal description of whole brain connectivity: A comparison of resting state MEG, fMRI, and DWI. Human Brain Mapping. 2015 Oct; 37(1):20–34. http://dx.doi.org/10.1002/hbm.22995, doi: 10.1002/hbm.22995.

Gutmann MU, Cor J, er. Bayesian Optimization for Likelihood-Free Inference of Simulator-Based Statistical Models. Journal of Machine Learning Research. 2016; 17(125):1–47. http://jmlr.org/papers/v17/15-017.html.

Haegens S, Cousijn H, Wallis G, Harrison PJ, Nobre AC. Inter- and intra-individual variability in alpha peak frequency. NeuroImage. 2014 May; 92:46–55. http://dx.doi.org/10.1016/j.neuroimage.2014.01.049, doi: 10.1016/j.neuroimage.2014.01.049.

Haque H, Lobier M, Palva JM, Palva S. Neuronal correlates of full and partial visual conscious perception. Consciousness and Cognition. 2020 Feb; 78:102863. https://doi.org/10.1016/j.concog.2019.102863, doi: 10.1016/j.concog.2019.102863.

Hardstone R, Poil SS, Schiavone G, Jansen R, Nikulin VV, Mansvelder HD, Linkenkaer-Hansen K. Detrended fluctuation analysis: a scale-free view on neuronal oscillations. Frontiers in physiology. 2012; 3:450.

Hashemi M, Vattikonda A, Sip V, Guye M, Bartolomei F, Woodman MM, Jirsa VK. The Bayesian Virtual Epileptic Patient: A probabilistic framework designed to infer the spatial map of epileptogenicity in a personalized large-scale brain model of epilepsy spread. NeuroImage. 2020; 217:116839.

Heggli OA, Cabral J, Konvalinka I, Vuust P, Kringelbach ML. A Kuramoto model of self-other integration across interpersonal synchronization strategies. PLOS Computational Biology. 2019 Oct; 15(10):e1007422. http://dx.doi.org/10.1371/journal.pcbi.1007422, doi: 10.1371/journal.pcbi.1007422.

Heiney K, Huse Ramstad O, Fiskum V, Christiansen N, Sandvig A, Nichele S, Sandvig I. Criticality, Connectivity, and Neural Disorder: A Multifaceted Approach to Neural Computation. Frontiers in Computational Neuroscience. 2021 Feb; 15. http://dx.doi.org/10.3389/fncom.2021.611183, doi: 10.3389/fncom.2021.611183.

Hirvonen J, Wibral M, Palva JM, Singer W, Uhlhaas P, Palva S. Whole-Brain Source-Reconstructed MEG-Data Reveal Reduced Long-Range Synchronization in Chronic Schizophrenia. eneuro. 2017 Sep; 4(5):ENEURO.0338–17.2017. http://dx.doi.org/10.1523/ENEURO.0338-17.2017, doi: 10.1523/eneuro.0338-17.2017.

Hobbs JP, Smith JL, Beggs JM. Aberrant Neuronal Avalanches in Cortical Tissue Removed From Juvenile Epilepsy Patients. Journal of Clinical Neurophysiology. 2010 Dec; 27(6):380–386. http://dx.doi.org/10.1097/WNP.0b013e3181fdf8d3, doi: 10.1097/wnp.0b013e3181fdf8d3.

Huber PJ. Robust Regression: Asymptotics, Conjectures and Monte Carlo. The Annals of Statistics. 1973 Sep; 1(5). http://dx.doi.org/10.1214/aos/1176342503, doi: 10.1214/aos/1176342503.

Ippolito G, Bertaccini R, Tarasi L, Di Gregorio F, Trajkovic J, Battaglia S, Romei V. The Role of Alpha Oscillations among the Main Neuropsychiatric Disorders in the Adult and Developing Human Brain: Evidence from the Last 10 Years of Research. Biomedicines. 2022 Dec; 10(12):3189. http://dx.doi.org/10.3390/biomedicines10123189, doi: 10.3390/biomedicines10123189.

Jenkinson M, Beckmann CF, Behrens TEJ, Woolrich MW, Smith SM. FSL. NeuroImage. 2012 Aug; 62(2):782–790. http://dx.doi.org/10.1016/j.neuroimage.2011.09.015, doi: 10.1016/j.neuroimage.2011.09.015.

Kaiser RH, Andrews-Hanna JR, Wager TD, Pizzagalli DA. Large-Scale Network Dysfunction in Major Depressive Disorder: A Meta-analysis of Resting-State Functional Connectivity. JAMA Psychiatry. 2015 Jun; 72(6):603. http://dx.doi.org/10.1001/jamapsychiatry.2015.0071, doi: 10.1001/jamapsychiatry.2015.0071.

Katsoulakis E, Wang Q, Wu H, Shahriyari L, Fletcher R, Liu J, Achenie L, Liu H, Jackson P, Xiao Y, Syeda-Mahmood T, Tuli R, Deng J. Digital twins for health: a scoping review. npj Digital Medicine. 2024 Mar; 7(1). http://dx.doi.org/10.1038/s41746-024-01073-0, doi: 10.1038/s41746-024-01073-0.

Kinouchi O, Copelli M. Optimal dynamical range of excitable networks at criticality. Nature Physics. 2006 Apr; 2(5):348–351. http://dx.doi.org/10.1038/nphys289, doi: 10.1038/nphys289.

Koller DP, Schirner M, Ritter P. Human connectome topology directs cortical traveling waves and shapes frequency gradients. Nature Communications. 2024 Apr; 15(1). http://dx.doi.org/10.1038/s41467-024-47860-x, doi: 10.1038/s41467-024-47860-x.

Korhonen O, Palva S, Palva JM. Sparse weightings for collapsing inverse solutions to cortical parcellations optimize M/EEG source reconstruction accuracy. Journal of Neuroscience Methods. 2014 Apr; 226:147–160. https://doi.org/10.1016/j.jneumeth.2014.01.031, doi: 10.1016/j.jneumeth.2014.01.031.

Kringelbach ML, Cruzat J, Cabral J, Knudsen GM, Carhart-Harris R, Whybrow PC, Logothetis NK, Deco G. Dynamic coupling of whole-brain neuronal and neurotransmitter systems. Proceedings of the National Academy of Sciences. 2020 Apr; 117(17):9566–9576. http://dx.doi.org/10.1073/pnas.1921475117, doi: 10.1073/pnas.1921475117.

Kuramoto Y. International symposium on mathematical problems in theoretical physics. Lecture notes in Physics. 1975; 30:420.

Lachaux JP, Rodriguez E, Martinerie J, Varela FJ. Measuring phase synchrony in brain signals. Human Brain Mapping. 1999; 8(4):194–208. http://dx.doi.org/10.1002/(sici)1097-0193(1999)8:4<194::aid-hbm4>3.0.co;2-c, doi: 10.1002/(sici)1097-0193(1999)8:4<194::aid-hbm4>3.0.co;2-c.

Laubenbacher R, Mehrad B, Shmulevich I, Trayanova N. Digital twins in medicine. Nature Computational Science. 2024 Mar; 4(3):184–191. http://dx.doi.org/10.1038/s43588-024-00607-6, doi: 10.1038/s43588-024-00607-6.

Linkenkaer-Hansen K, Nikouline VV, Palva JM, Ilmoniemi RJ. Long-Range Temporal Correlations and Scaling Behavior in Human Brain Oscillations. The Journal of Neuroscience. 2001 Feb; 21(4):1370–1377. https://doi.org/10.1523/jneurosci.21-04-01370.2001, doi: 10.1523/jneurosci.21-04-01370.2001.

Linkenkaer-Hansen K, Nikouline VV, Palva JM, Ilmoniemi RJ. Long-range temporal correlations and scaling behavior in human brain oscillations. Journal of Neuroscience. 2001; 21(4):1370–1377.

Lintusaari J, Gutmann MU, Dutta R, Kaski S, Corander J. Fundamentals and Recent Developments in Approximate Bayesian Computation. Systematic Biology. 2016 Oct; p. syw077. http://dx.doi.org/10.1093/sysbio/syw077, doi: 10.1093/sysbio/syw077.

Liu X, Reynolds AC. A multiobjective steepest descent method with applications to optimal well control. Computational Geosciences. 2016; 20:355–374.

Liu Y, Dahmen KA. Unexpected universality in static and dynamic avalanches. Physical Review E. 2009 Jun; 79(6). http://dx.doi.org/10.1103/PhysRevE.79.061124, doi: 10.1103/physreve.79.061124.

Lotfi N, Feliciano T, Aguiar LAA, Silva TPL, Carvalho TTA, Rosso OA, Copelli M, Matias FS, Carelli PV. Statistical complexity is maximized close to criticality in cortical dynamics. Physical Review E. 2021 Jan; 103(1). http://dx.doi.org/10.1103/PhysRevE.103.012415, doi: 10.1103/physreve.103.012415.

Manning JR, Jacobs J, Fried I, Kahana MJ. Broadband Shifts in Local Field Potential Power Spectra Are Correlated with Single-Neuron Spiking in Humans. The Journal of Neuroscience. 2009 Oct; 29(43):13613–13620. http://dx.doi.org/10.1523/JNEUROSCI.2041-09.2009, doi: 10.1523/jneurosci.2041-09.2009.

Mazzoni A, Panzeri S, Logothetis NK, Brunel N. Encoding of Naturalistic Stimuli by Local Field Potential Spectra in Networks of Excitatory and Inhibitory Neurons. PLoS Computational Biology. 2008 Dec; 4(12):e1000239. http://dx.doi.org/10.1371/journal.pcbi.1000239, doi: 10.1371/journal.pcbi.1000239.

Messaritaki E, Foley S, Schiavi S, Magazzini L, Routley B, Jones DK, Singh KD. Predicting MEG resting-state functional connectivity from microstructural information. Network Neuroscience. 2021; 5(2):477–504. http://dx.doi.org/10.1162/netn_a_00187, doi: 10.1162/netn_a_00187.

Micou C, O'Leary T. Representational drift as a window into neural and behavioural plasticity. Current Opinion in Neurobiology. 2023 Aug; 81:102746. http://dx.doi.org/10.1016/j.conb.2023.102746, doi: 10.1016/j.conb.2023.102746.

Mohammadi Y, Moradi MH. Prediction of Depression Severity Scores Based on Functional Connectivity and Complexity of the EEG Signal. Clinical EEG and Neuroscience. 2020 Oct; 52(1):52–60. http://dx.doi.org/10.1177/1550059420965431, doi: 10.1177/1550059420965431.

Muñoz MA. Colloquium: Criticality and dynamical scaling in living systems. Reviews of Modern Physics. 2018 Jul; 90(3). http://dx.doi.org/10.1103/RevModPhys.90.031001, doi: 10.1103/revmodphys.90.031001.

Myrov V, Siebenhühner F, Juvonen JJ, Arnulfo G, Palva S, Palva JM. Rhythmicity of neuronal oscillations delineates their cortical and spectral architecture. Communications Biology. 2024 Apr; 7(1). http://dx.doi.org/10.1038/s42003-024-06083-y, doi: 10.1038/s42003-024-06083-y.

Nolte G, Aburidi M, Engel AK. Robust calculation of slopes in detrended fluctuation analysis and its application to envelopes of human alpha rhythms. Scientific Reports. 2019 Apr; 9(1). https://doi.org/10.1038/s41598-019-42732-7, doi: 10.1038/s41598-019-42732-7.

Ódor G, Kelling J. Critical synchronization dynamics of the Kuramoto model on connectome and small world graphs. Scientific reports. 2019; 9(1):19621.

Oesterle J, Behrens C, Schröder C, Hermann T, Euler T, Franke K, Smith RG, Zeck G, Berens P. Bayesian inference for biophysical neuron models enables stimulus optimization for retinal neuroprosthetics. eLife. 2020 Oct; 9. http://dx.doi.org/10.7554/eLife.54997, doi: 10.7554/elife.54997.

Palva JM, Monto S, Kulashekhar S, Palva S. Neuronal synchrony reveals working memory networks and predicts individual memory capacity. Proceedings of the National Academy of Sciences. 2010 Apr; 107(16):7580–7585. http://dx.doi.org/10.1073/pnas.0913113107, doi: 10.1073/pnas.0913113107.

Palva JM, Palva S, Kaila K. Phase Synchrony among Neuronal Oscillations in the Human Cortex. Journal of Neuroscience. 2005; 25(15):3962–3972. doi: 10.1523/JNEUROSCI.4250-04.2005.

Palva JM, Zhigalov A, Hirvonen J, Korhonen O, Linkenkaer-Hansen K, Palva S. Neuronal long-range temporal correlations and avalanche dynamics are correlated with behavioral scaling laws. Proceedings of the National Academy of Sciences. 2013 Feb; 110(9):3585–3590. https://doi.org/10.1073/pnas.1216855110, doi: 10.1073/pnas.1216855110.

Palva S, Monto S, Palva JM. Graph properties of synchronized cortical networks during visual working memory maintenance. NeuroImage. 2010 Feb; 49(4):3257–3268. http://dx.doi.org/10.1016/j.neuroimage.2009.11.031, doi: 10.1016/j.neuroimage.2009.11.031.

Pang JC, Gollo LL, Roberts JA. Stochastic synchronization of dynamics on the human connectome. NeuroImage. 2021 Apr; 229:117738. http://dx.doi.org/10.1016/j.neuroimage.2021.117738, doi: 10.1016/j.neuroimage.2021.117738.

Poil SS, Hardstone R, Mansvelder HD, Linkenkaer-Hansen K. Critical-State Dynamics of Avalanches and Oscillations Jointly Emerge from Balanced Excitation/Inhibition in Neuronal Networks. Journal of Neuroscience. 2012 Jul; 32(29):9817–9823. http://dx.doi.org/10.1523/JNEUROSCI.5990-11.2012, doi: 10.1523/jneurosci.5990-11.2012.

Ponce-Alvarez A, Deco G. The Hopf whole-brain model and its linear approximation. Scientific Reports. 2024 Jan; 14(1). http://dx.doi.org/10.1038/s41598-024-53105-0, doi: 10.1038/s41598-024-53105-0.

Pusil S, López ME, Cuesta P, Bruna R, Pereda E, Maestu F. Hypersynchronization in mild cognitive impairment: the 'X'model. Brain. 2019; 142(12):3936–3950.

Ritter P, Schirner M, McIntosh AR, Jirsa VK. The Virtual Brain Integrates Computational Modeling and Multimodal Neuroimaging. Brain Connectivity. 2013 Apr; 3(2):121–145. http://dx.doi.org/10.1089/brain.2012.0120, doi: 10.1089/brain.2012.0120.

Roberts JA, Gollo LL, Abeysuriya RG, Roberts G, Mitchell PB, Woolrich MW, Breakspear M. Metastable brain waves. Nature Communications. 2019 Mar; 10(1). http://dx.doi.org/10.1038/s41467-019-08999-0, doi: 10.1038/s41467-019-08999-0.

San O. The digital twin revolution. Nature Computational Science. 2021 May; 1(5):307–308. http://dx.doi.org/10.1038/s43588-021-00077-0, doi: 10.1038/s43588-021-00077-0.

Schaefer A, Kong R, Gordon EM, Laumann TO, Zuo XN, Holmes AJ, Eickhoff SB, Yeo BT. Local-global parcellation of the human cerebral cortex from intrinsic functional connectivity MRI. Cerebral cortex. 2018; 28(9):3095–3114.

Schirner M, Deco G, Ritter P. Learning how network structure shapes decision-making for bio-inspired computing. Nature Communications. 2023; 14(1):2963.

Schmidt R, Ruiz MH, Kilavik BE, Lundqvist M, Starr PA, Aron AR. Beta Oscillations in Working Memory, Executive Control of Movement and Thought, and Sensorimotor Function. The Journal of Neuroscience. 2019 Oct; 39(42):8231–8238. https://doi.org/10.1523/jneurosci.1163-19.2019, doi: 10.1523/jneurosci.1163-19.2019.

Schmidt R, LaFleur KJ, de Reus MA, van den Berg LH, van den Heuvel MP. Kuramoto model simulation of neural hubs and dynamic synchrony in the human cerebral connectome. BMC neuroscience. 2015; 16(1):1–13.

Shew WL, Plenz D. The Functional Benefits of Criticality in the Cortex. The Neuroscientist. 2012 May; 19(1):88–100. http://dx.doi.org/10.1177/1073858412445487, doi: 10.1177/1073858412445487.

Shine JM, Müller EJ, Munn B, Cabral J, Moran RJ, Breakspear M. Computational models link cellular mechanisms of neuromodulation to large-scale neural dynamics. Nature Neuroscience. 2021 May; 24(6):765–776. http://dx.doi.org/10.1038/s41593-021-00824-6, doi: 10.1038/s41593-021-00824-6.

Shirai S, Acharya SK, Bose SK, Mallinson JB, Galli E, Pike MD, Arnold MD, Brown SA. Long-range temporal correlations in scale-free neuromorphic networks. Network Neuroscience. 2020 Jan; 4(2):432–447. http://dx.doi.org/10.1162/netn_a_00128, doi: 10.1162/netn_a_00128.

Siebenhühner F, Palva JM, Palva S. Node centrality in MEG resting-state networks co-varies with neurotransmitter receptor and transporter density. bioRxiv. 2024 Jan; http://dx.doi.org/10.1101/2024.01.11.575176, doi: 10.1101/2024.01.11.575176.

Siebenhühner F, Wang SH, Arnulfo G, Lampinen A, Nobili L, Palva JM, Palva S. Genuine cross-frequency coupling networks in human resting-state electrophysiological recordings. PLOS Biology. 2020 May; 18(5):e3000685. http://dx.doi.org/10.1371/journal.pbio.3000685, doi: 10.1371/journal.pbio.3000685.

Siebenhühner F, Wang SH, Arnulfo G, Lampinen A, Nobili L, Palva JM, Palva S. Genuine cross-frequency coupling networks in human resting-state electrophysiological recordings. PLOS Biology. 2020 May; 18(5):e3000685. https://doi.org/10.1371/journal.pbio.3000685, doi: 10.1371/journal.pbio.3000685.

Siebenhühner F, Wang SH, Palva JM, Palva S. Cross-frequency synchronization connects networks of fast and slow oscillations during visual working memory maintenance. eLife. 2016 Sep; 5. http://dx.doi.org/10.7554/eLife.13451, doi: 10.7554/elife.13451.

Simola J, Siebenhühner F, Myrov V, Kantojärvi K, Paunio T, Palva JM, Brattico E, Palva S. Genetic polymorphisms in COMT and BDNF influence synchronization dynamics of human neuronal oscillations. iScience. 2022 Sep; 25(9):104985. http://dx.doi.org/10.1016/j.isci.2022.104985, doi: 10.1016/j.isci.2022.104985.

Smith RE, Tournier JD, Calamante F, Connelly A. Anatomically-constrained tractography: improved diffusion MRI streamlines tractography through effective use of anatomical information. Neuroimage. 2012; 62(3):1924–1938.

Smith RE, Tournier JD, Calamante F, Connelly A. SIFT: Spherical-deconvolution informed filtering of tractograms. Neuroimage. 2013; 67:298–312.

Tournier JD, Calamante F, Connelly A. Robust determination of the fibre orientation distribution in diffusion MRI: non-negativity constrained super-resolved spherical deconvolution. Neuroimage. 2007; 35(4):1459–1472.

Tournier JD, Smith R, Raffelt D, Tabbara R, Dhollander T, Pietsch M, Christiaens D, Jeurissen B, Yeh CH, Connelly A. MRtrix3: A fast, flexible and open software framework for medical image processing and visualisation. NeuroImage. 2019 Nov; 202:116137. http://dx.doi.org/10.1016/j.neuroimage.2019.116137, doi: 10.1016/j.neuroimage.2019.116137.

Villegas P, Moretti P, Muñoz MA. Frustrated hierarchical synchronization and emergent complexity in the human connectome network. Scientific Reports. 2014 Aug; 4(1). http://dx.doi.org/10.1038/srep05990, doi: 10.1038/srep05990.

Vinck M, Oostenveld R, van Wingerden M, Battaglia F, Pennartz CMA. An improved index of phase-synchronization for electrophysiological data in the presence of volume-conduction, noise and sample-size bias. NeuroImage. 2011 Apr; 55(4):1548–1565. https://doi.org/10.1016/j.neuroimage.2011.01.055, doi: 10.1016/j.neuroimage.2011.01.055.

Wang P, Kong R, Kong X, Liégeois R, Orban C, Deco G, Van Den Heuvel MP, Thomas Yeo B. Inversion of a large-scale circuit model reveals a cortical hierarchy in the dynamic resting human brain. Science advances. 2019; 5(1):eaat7854.

Wang SH, Arnulfo G, Nobili L, Myrov V, Ferrari P, Ciuciu P, Palva S, Palva JM. Neuronal Synchrony and Critical Bistability: Mechanistic Biomarkers for Localizing the Epileptogenic Network. preprint. 2023 May; http://dx.doi.org/10.1101/2023.05.21.541570, doi: 10.1101/2023.05.21.541570.

Wang SH, Lobier M, Siebenhühner F, Puoliväli T, Palva S, Palva JM. Hyperedge bundling: A practical solution to spurious interactions in MEG/EEG source connectivity analyses. NeuroImage. 2018 Jun; 173:610–622. https://doi.org/10.1016/j.neuroimage.2018.01.056, doi: 10.1016/j.neuroimage.2018.01.056.

Wang SH, Siebenhühner F, Arnulfo G, Myrov V, Nobili L, Breakspear M, Palva S, Palva JM. Critical-like Brain Dynamics in a Continuum from Second- to First-Order Phase Transition. The Journal of Neuroscience. 2023 Oct; 43(45):7642–7656. http://dx.doi.org/10.1523/JNEUROSCI.1889-22.2023, doi: 10.1523/jneurosci.1889-22.2023.

Wang XJ. Macroscopic gradients of synaptic excitation and inhibition in the neocortex. Nature Reviews Neuroscience. 2020 Feb; 21(3):169–178. http://dx.doi.org/10.1038/s41583-020-0262-x, doi: 10.1038/s41583-020-0262-x.

Williams N, Ojanperä A, Siebenhühner F, Toselli B, Palva S, Arnulfo G, Kaski S, Palva JM. The influence of inter-regional delays in generating large-scale brain networks of phase synchronization. NeuroImage. 2023 Oct; 279:120318. http://dx.doi.org/10.1016/j.neuroimage.2023.120318, doi: 10.1016/j.neuroimage.2023.120318.

Yeo BT, Krienen FM, Sepulcre J, Sabuncu MR, Lashkari D, Hollinshead M, Roffman JL, Smoller JW, Zöllei L, Polimeni JR, et al. The organization of the human cerebral cortex estimated by intrinsic functional connectivity. Journal of neurophysiology. 2011; .

Zhang S, Chen Jm, Kuang L, Cao J, Zhang H, Ai M, Wang W, Zhang Sd, Wang Sy, Liu Sj, Fang Wd. Association between abnormal default mode network activity and suicidality in depressed adolescents. BMC Psychiatry. 2016 Sep; 16(1). http://dx.doi.org/10.1186/s12888-016-1047-7, doi: 10.1186/s12888-016-1047-7.

Ziaeemehr A, Valizadeh A. Frequency-Resolved Functional Connectivity: Role of Delay and the Strength of Connections. Frontiers in Neural Circuits. 2021 Mar; 15. https://doi.org/10.3389/fncir.2021.608655, doi: 10.3389/fncir.2021.608655.

Zimmern V. Why Brain Criticality Is Clinically Relevant: A Scoping Review. Frontiers in Neural Circuits. 2020 Aug; 14. http://dx.doi.org/10.3389/fncir.2020.00054, doi: 10.3389/fncir.2020.00054.

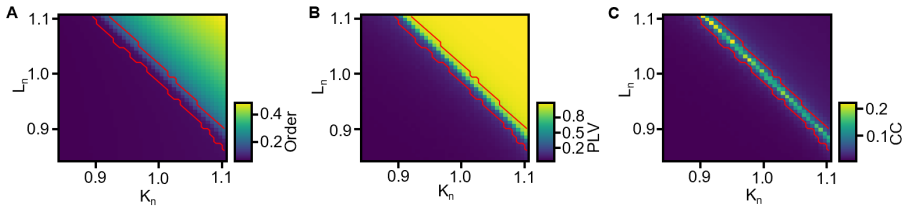

Figure S1. A,B,C An average model order (**A**), PLV (**B**) and CC (**C**).

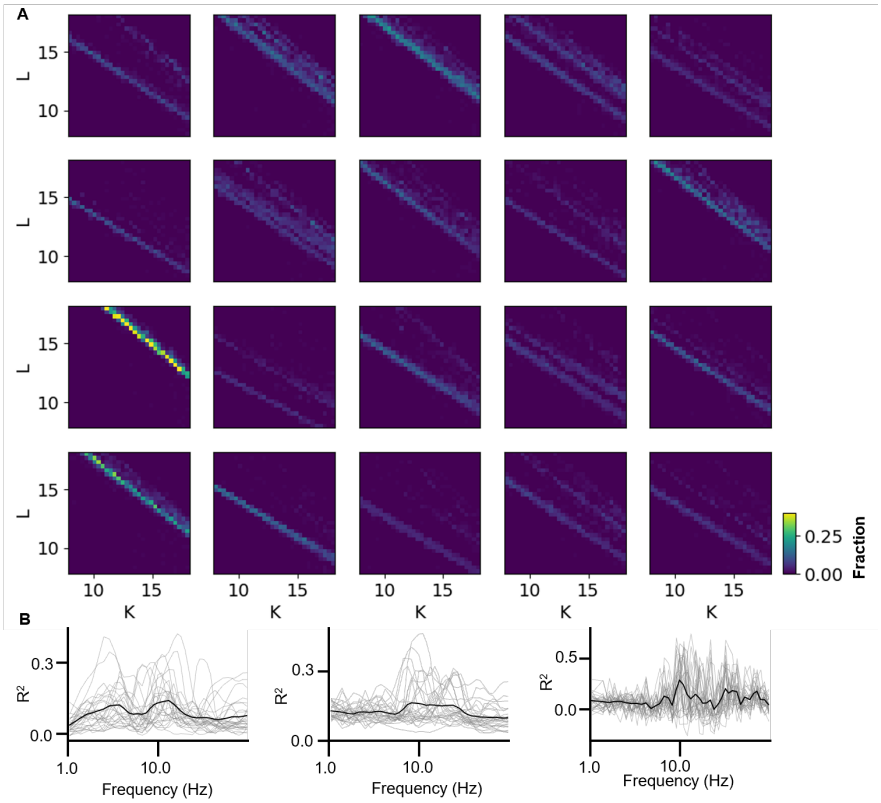

Figure S2. A A fraction of nodes with DFA $>= 0.7$ for models based on individual structural connectome. **B** R^2 between predicted and actual PS matrices (left), DFA (middle) and pACF (right) as a function of frequency.

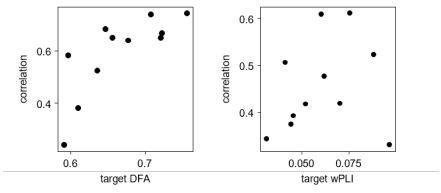

Figure S3. A correlation between predicted and target phase synchrony (left) and DFA (right) as a function of the target metric value.